Control Engineering Practice 94 (2020) 104199

Contents lists available at ScienceDirect

Control Engineering Practice

journal homepage: www.elsevier.com/locate/conengprac

Modeling the thermal and soot oxidation dynamics inside a ceria-coated gasoline particulate filter

Harikesh Arunachalam [a], Gabriele Pozzato [b], Mark A. Hoffman [c], Simona Onori [a,*]

[a] Department of Energy Resources Engineering, Stanford University, Stanford, CA 94305, USA
[b] Dipartimento di Elettronica, Informazione e Bioingegneria, Politecnico di Milano, 20133 Milano, Italy
[c] Department of Mechanical Engineering, Auburn University, Auburn, AL 36849, USA

ARTICLE INFO

Keywords:
Gasoline direct injection
gasoline particulate filter
catalytic washcoat
particle swarm optimization
experimental validation

ABSTRACT

Gasoline particulate filters (GPFs) are practically adoptable devices to mitigate particulate matter emissions from vehicles using gasoline direct ignition engines. This paper presents a newly developed control-oriented model to characterize the thermal and soot oxidation dynamics in a ceria-coated GPF. The model utilizes the GPF inlet exhaust gas temperature, exhaust gas mass flow rate, the initial GPF soot loading density, and air–fuel ratio to predict the internal GPF temperature and the amount of soot oxidized during regeneration events. The reaction kinetics incorporated in the model involve the rates of both oxygen- and ceria-initiated soot oxidation reactions. Volumetric model parameters are calculated from the geometric information of the coated GPF, while the air–fuel ratio is used to determine the volume fractions of the exhaust gas constituents. The exhaust gas properties are evaluated using the volume fractions and thermodynamic tables, while the cordierite specific heat capacity is identified using a *clean* experimental data set. The enthalpies of the regeneration reactions are calculated using thermochemical tables. Physical insights from the proposed model are thus enhanced by limiting the number of parameters obtained from fitting to only those which cannot be directly measured from experiments. The parameters of the model are identified using the particle swarm optimization algorithm and a cost function designed to simultaneously predict both thermal and soot oxidation dynamics. Parameter identification and model validation are performed using independent data sets from laboratory experiments conducted on a ceria-coated GPF. This work demonstrates that the proposed model can be successfully implemented to predict ceria-coated GPF dynamics under different soot loading and temperature conditions.

1. Introduction

Rapid urbanization and industrialization in recent decades has been achieved through excessive consumption of carbon-based energy resources. These advancements though come at the cost of environmental degradation (Zaman & Abd-el Moemen, 2017). Energy policies are being enforced in the transport sector that involve promoting sustainable transportation by enhancing vehicle electrification and alternate sources of propulsion (Wu et al., 2017).

A notable advancement in engine technology to meet current and future regulation targets is the transition from port fuel injection (PFI) engines to gasoline direct injection (GDI) engines (National Research Council, 2011). In PFI engines, fuel is sprayed into the intake ports where it mixes with the incoming air, whereas in GDI engines, fuel is sprayed directly into the engine cylinder where it atomizes, mixes with the incoming air, and evaporates. Because of thermodynamic benefits and flexibility in fuel injection, GDI engines improve combustion efficiency, enhance fuel economy, increase power output, and reduce greenhouse gas emissions in comparison with PFI systems (Zhu et al., 2016).

One of the drawbacks of GDI engines is that they suffer from limited mixing of air and fuel inside the combustion chamber under certain operating modes. As a result, hazardous particulate matter (PM) are released into the atmosphere through the exhaust (Khalek, Bougher, & Jetter, 2010). Experimental studies have shown that GDI engines emit greater quantities of PM emissions than PFI engines (Johnson & Joshi, 2017; Zhu et al., 2016).

Aftertreatment devices, such as Gasoline Particulate Filters (GPF), are today considered the most promising and practically adoptable solution to limit PM/PN out of GDI exhaust (Mamakos, Martini, Dilara, & Drossinos, 2011).

Particulate filters have been successfully implemented in diesel vehicles through diesel particulate filters (DPFs) (Yang, Deng, Gao, & He, 2016). GPFs and DPFs have similar geometric structures. The stoichiometric combustion of gasoline results in exhaust gases having

* Corresponding author.
E-mail address: sonori@stanford.edu (S. Onori).

https://doi.org/10.1016/j.conengprac.2019.104199
Received 19 February 2019; Received in revised form 19 September 2019; Accepted 15 October 2019
Available online 5 November 2019
0967-0661/

Nomenclature

$\Delta H_{C,1}$	Endothermic catalytic reaction enthalpy, [J/mol]
$\Delta H_{C,2}$	Exothermic catalytic reaction enthalpy, [J/mol]
ΔH_T	Exothermic soot oxidation reaction enthalpy, [J/mol]
λ	Air/fuel ratio normalized by the stoichiometric air/fuel ratio, [−]
ϕ_{wall}	Average porosity of the wall in the coated GPF channels, [−]
ρ_{GPF}	Particulate filter density, 1100 [kg/m^3]
ρ_{O_2}	Density of oxygen, [kg/m^3]
ρ_{soot}	Initial soot loading density, [g/l]
$A_{C,1}$	Pre-exponential factor for the endothermic ceria reaction, [1/s]
$A_{C,2}$	Pre-exponential factor for the exothermic ceria reaction, [1/s]
A_T	Pre-exponential factor for the standard soot oxidation reaction, [1/s]
CO_{in}	Pre-GPF ppm levels of CO, [−]
CO_{out}	Post-GPF ppm levels of CO, [−]
$CO_{2,in}$	Pre-GPF ppm levels of CO_2, [−]
$CO_{2,out}$	Post-GPF ppm levels of CO_2, [−]
$C_{p,cord}$	Specific heat capacity of the cordierite GPF, [J/(kgK)]
$C_{p,gas}$	Specific heat capacity of the exhaust gas, [J/(kgK)]
D	Coated GPF substrate diameter, [m]
$E_a^{C,1}$	Endothermic catalytic reaction activation energy, [J/mol]
$E_a^{C,2}$	Exothermic catalytic reaction activation energy, [J/mol]
E_a^T	Exothermic soot oxidation reaction activation energy, [J/mol]
F	Total number of regeneration events in one data set, [−]
$h_{channel}$	Width of each channel, [m]
h_{plug}	Width of each plug, [m]
h_{wall}	Thickness of the wall, [m]
J	Cost function, [−]
k_T	Rate constant of the oxygen-initiated C to CO_2 reaction, [1/s]
l_{wall}	Length of the coated GPF substrate, [m]
l_{plug}	Length of each plug in the channels of the coated GPF, [m]
$m_{c,exp}$	Experimentally determined mass of soot, [kg]
$m_{c,GPF}$	Predicted mass of soot, [kg]
$m_{c,init}$	Initial mass of soot prior to regeneration, [kg]
m_{GPF}	Total mass of cordierite in the coated GPF, [kg]
m_{O_2}	Mass of oxygen, [kg]
$\dot{m}_g$	Measured exhaust gas mass flow rate, [kg/s]
M_C	Carbon molar mass, 12×10^{-3} [kg/mol]
M_{CO_2}	Carbon dioxide molar mass, 44×10^{-3} [kg/mol]
M_{O_2}	Oxygen molar mass, 32×10^{-3} [kg/mol]
n_C	Number of moles of carbon, [−]
n_{O_2}	Number of moles of oxygen, [−]
n_{total}	Total moles of the products of the combustion reaction, [mol]
N	Total number of data samples used to evaluate the cost function, [−]
N_{ch}	Total number of channels in the GPF, [−]
N_{cross}	Total number of channels across the semi-circular GPF section, [−]
ppm	Parts per million
PSO	Particle swarm optimization
Q_1	Exhaust gas convective heat transport, [J/s]
Q_2	Coated GPF ceramic substrate heat conduction, [J/s]
Q_{Reac}	Net heat of the regeneration reactions, [J/s]
R	Ideal gas constant, 8.314 [J/(molK)]
$R_{C,1}$	Rate of the endothermic ceria reaction, [mol/s]
$R_{C,2}$	Rate of the exothermic ceria reaction, [mol/s]
R_T	Rate of the standard soot oxidation reaction, [mol/s]
RMS	Root mean square
RMS_T	Percentage RMS error for the prediction of thermal dynamics, [−]
RMS_S	Percentage RMS error for the prediction of soot oxidation dynamics, [−]
SLD	Soot loading density, [g/l]
t_f	End time of a regeneration event, [s]
t_m	Time when the pre-GPF air–fuel ratio first reaches its maximum value, [s]
t_s	Start time of a regeneration event, [s]
T_4	Measured temperature at the axial mid-location of the GPF
T_{avg}	Average temperature of the GPF, calculated from measurements, [K]
T_{gas}	Temperature of the exhaust gas constituents, [K]
T_{inlet}	Measured exhaust gas temperature at the inlet of the GPF, [K]
T_{outlet}	Temperature of the exhaust gas leaving the GPF, [K]
T_{GPF}	Predicted average temperature of the GPF, [K]
V_{cord}	Total volume of cordierite in the GPF, 0.1828×10^{-3} [m^3]
V_{exh}	filter trapping volume, 1.222×10^{-3} [m^3]
Z_{CeO_2}	volume fraction of ceria, [−]
Y_{O_2}	volume fraction of oxygen, [−]

higher temperatures and lower oxygen content than diesel engine exhaust (Chan et al., 2012) thus resulting in different PM morphology. Additionally, gasoline engines typically inject fuel well in advance of the combustion event, facilitating adequate atomization and nearly homogeneous fuel–air mixing. This results in the formation of smaller particulates relative to diesel combustion (Whitaker, Kapus, Ogris, & Hollerer, 2011) and holistically alters the filtration behavior of the device. Transferring the DPF knowledge *as is* into GPF systems could be a misleading practice.

An abundance of literature has been published on DPFs, from experimental investigations across diverse operating conditions, model development ranging from lumped parameter strategies (Chiatti, Chiavola, & Falcucci, 2008; Depcik, Langness, & Mattson, 2014) to comprehensive physics-based models (Hassanpour & McPhee, 2018; Kostoglou & Konstandopoulos, 2005). There is comparatively less published literature on experimental investigations and modeling tools characterizing exhaust gas behavior in GPFs. This paper is, to the best of our knowledge, the first to proposed a physically-motivated lumped

parameter model, along with experimental identification, of a ceria coated GPF.

One of the challenges in characterizing GPF dynamics is a comprehensive understanding of the filtration and regeneration mechanisms that both highly depend on its internal temperature distribution. Mathematical models are used as *virtual sensors* to monitor GPF internal temperature behavior. This is what motivates this work.

Boger, Rose, Nicolin, Gunasekaran, and Glasson (2015) and Nicolin, Rose, Kunath, and Boger (2015) presented reduced-order models to investigate the thermal dynamics in uncoated GPFs. These models incorporate the C to CO_2 soot oxidation reaction, initiated by the presence of excess O_2 in the GPF during regeneration events. Opitz, Drochner, Vogel, and Votsmeier (2014) proposed a 1-D + 1-D model for a single channel GPF and assessed the cold-start performance of an uncoated GPF. Liu, Kim, Chanko, Lambert, and Pakko (2017) presented a mathematical model to determine the backpressure and filtration efficiency of metallic fibrous GPFs for design optimization purposes. Pozzato, Hoffman, and Onori (2017) developed a high fidelity 2-D model to characterize mass, energy, and momentum transport of exhaust gases inside an uncoated, clean GPF.

Recently, Korneev and Onori (2018) presented a new hybrid high-fidelity model describing the flow and the particulate transport of a wall-flow gasoline particulate filter.

Recent advancements have led to the development of filters with a catalytic washcoat applied across the channels of the GPF. These washcoat materials are generally inorganic oxides such as cerium oxide or precious metals such as platinum and rhodium (Morgan, 2015). Coated GPFs have been experimentally proven to offer significant advantages over uncoated GPFs such as: (a) 20–30% improvement in the filtration efficiency (Lambert, Chanko, Dobson, Liu, & Pakko, 2017), (b) 12% reduction in NO_x emissions (Morgan, 2015), and (c) enhanced soot oxidation capability under relatively lower GPF temperatures (Morgan, 2015).

Regeneration mechanisms, which oxidize soot particulates at elevated temperatures in the presence of oxygen, must be clearly understood for two reasons: (a) monitoring temperature to prevent internal thermal stresses, and (b) developing control strategies to minimize emissions through optimal active regeneration. The work presented in Arunachalam, Pozzato, Hoffman, and Onori (2017) characterizes the thermal dynamics in a ceria-coated GPF through a physics-based thermal model to predict the convective heat transport of the exhaust gas and the thermal inertia of the GPF. The drawback of Arunachalam et al. (2017) was in the large parameter set to identify, which was left to a brute force based method.

In this paper, the ceria-coated GPF system is modeled by accounting for convective heat transport dynamics, the C to CO_2 oxidation reactions, and ceria-initiated catalytic reactions to predict the amount of heat generated during regeneration and a subset of the model parameters are obtained by direct computation from reaction enthalpies values, geometric design specifications, and using new set of experimental data, *e.g.*, *clean data set prior to soot accumulation* to identify the specific heat capacity of the cordierite GPF, $C_{p,cord}$. Furthermore, the identification of the remaining subset of parameters is conducted by considering three different cost functions and newly collected experimental data.

This paper is structured as follows: Section 2 presents the GPF system, Section 3 describes the mathematical formulation of the thermal energy balance equation, the soot consumption dynamic equation, and the formation–consumption dynamic equation of active ceria sites for carbon interaction. Supported by experimental evidence, a reduction of the modeling framework is proposed in which only reactions that lead to the conversion of C to CO_2 are considered. Section 4 outlines the experimental characterization of the ceria-coated GPF investigated in this study, and the parameter identification study using a *combined* cost function to determine the cordierite specific heat capacity, the exponential factor, and activation energy of the regeneration reactions. Section 5 elaborates upon the validation and predictiveness of the proposed modeling framework. Finally, Section 6 summarizes the contributions of this work. Appendix A outlines the determination of the volumetric model parameters, Appendix B elaborate upon the determination of the exhaust gas properties that are incorporated in the model, Appendix C describes the approach to determine the amount of soot oxidized during a regeneration event, and Appendix D summarize the results of the parameter identification study using a *thermal* and *soot* cost function.

2. Gasoline particulate filters

GPFs are emissions aftertreatment devices installed in the tailpipe of GDI operating vehicles to mitigate particulate emissions. GPF substrates are generally composed of a porous three-dimensional structure (Gong et al., 2018) and are made of ceramic materials or metallic fibers. They have been synthesized in a variety of shapes ranging from circular to oval cross section (Williams, 2001).

GPFs consist of a monolithic structure with axially parallel channels which are alternatively plugged at each end. As the exhaust gas enters the inlet channel and is forced to pass through the porous walls, soot particles are trapped within the channel walls. Over time, this accumulation of soot increases the engine back pressure, which can negatively impact engine performance and fuel economy. To minimize this negative impact, the soot trapped in the GPF must be periodically removed. This is accomplished via regeneration, i.e. oxidation of soot at elevated temperatures in the presence of oxygen (Nicolin et al., 2015).

The structure and internal design of the coated GPF used in the experimental campaign of this work is presented in Fig. 1. The washcoat material is primarily composed of ceria (CeO_2). Precious metals are loaded within the cerium to provide catalytic reaction benefits, while the cerium provides the scaffolding for the precious metals and oxygen storage ability that enhance soot oxidation reactions inside the GPF.

3. Temperature and soot oxidation modeling of a ceria-coated GPF

This section presents the development of the model to characterize the thermal and soot oxidation dynamics inside a ceria-coated GPF. Reaction rate expressions are formulated to quantify heat generation and species concentrations within the GPF during a regeneration event. Soot oxidation dynamics and the formation–consumption dynamics of active ceria sites are determined using the reaction rate expressions. Apart from reaction kinetics, heat is transported to and from the GPF due to the exhaust gas flow, and the cordierite thermal inertia that governs the volumetric absorption of heat by the GPF dictates the time rate of change in GPF temperature. Fig. 2 summarizes the proposed GPF modeling in terms of inputs, outputs, and state variables.

3.1. Soot oxidation reaction kinetics

We can distinguish between volatile and nonvolatile PM (Rounce, Brogan, & Eastwood, 2013). Volatile constituents are composed of sulphate, nitrate, and organic compounds, while non-volatile constituents are primarily composed of carbon soot and ash. In GPFs, ash accumulates primarily because of engine oils. The accumulation of these particles affects the pressure drop and causes plugging of the filter. Similarly for DPF, ash represents an aging factor (Ito et al., 2015; Shimoda et al., 2012). However, if compared to temperature and soot oxidation, ash deposition occurs over a different time scale, characterized by slow dynamics. Thus, without any loss of generality, ash loading can be neglected for the purpose of this work. Moreover, the equations presented in this work do not consider any dynamics associated with the volatile constituents. The oxidation reactions in the model, involving only the carbonaceous soot particles, generally results in the formation of either carbon monoxide (CO) or carbon

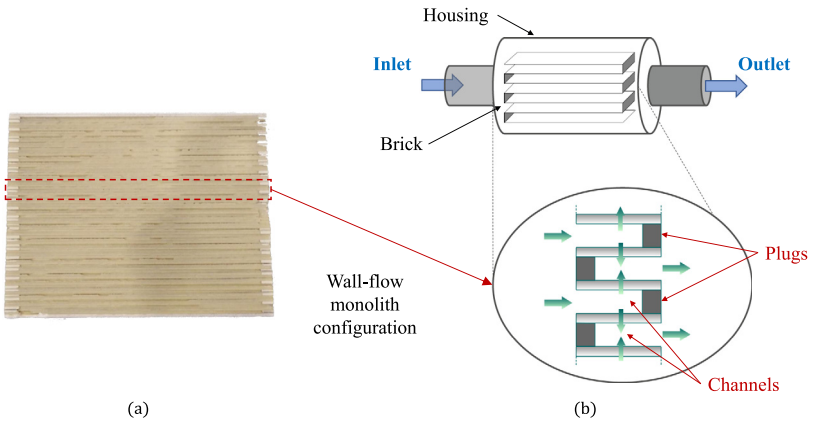

Fig. 1. (a) Side view of the sectioned coated GPF, and (b) axially parallel channels which are alternatively plugged at each end with cordierite. A two-dimensional view of an inlet channel, porous wall, and an outlet channel of the GPF is shown here.

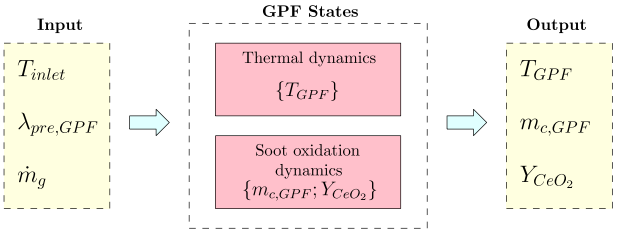

Fig. 2. Control-oriented model scheme. The GPF is described in terms of thermal and soot oxidation dynamics. The inputs of the model are the measured exhaust gas temperature (T_{inlet}), the pre-GPF air/fuel ratio ($\lambda_{pre,GPF}$), and the exhaust gas mass flow rate ($\dot{m}_g$). The states, which coincides with the measured outputs are the average GPF temperature (T_{GPF}), the soot mass ($m_{c,GPF}$), and the volume fraction of ceria (Z_{CeO_2}). The formal state-space representation of the lumped GPF model is provided in Takahashi, Korneev, and Onori (2019).

dioxide (CO_2), depending upon the amount of oxygen available during the reaction (Nicolin et al., 2015):

$$\begin{cases} C + O_2 \rightarrow CO_2 \\ C + 0.5O_2 \rightarrow CO \end{cases} \quad \textbf{Exothermic} \tag{1}$$

The above oxygen-initiated soot oxidation reactions compete against each other during regeneration. This represents an important modeling challenge since information regarding the relative dominance of CO_2 formation reactions over CO formation reactions, or vice-versa, is unavailable. As a result, quantification of the competition between these reactions becomes complex. For the proposed lumped modeling approach, this challenge can be addressed if there is evidence to prove that the concentration of one of the products of these two reactions (CO or CO_2) is significantly higher than the other.

Fig. 3 shows the variation of the experimentally measured pre- and post-GPF ppm levels of CO and CO_2. The shaded region represents the course of a regeneration event. During regeneration, the GPF inlet CO ppm levels ($\approx 50-100$) are significantly lower than the CO_2 ppm levels (of the order of 10^4). It is also observed that the CO ppm level post-GPF is zero. This result is not a surprise as CO is typically an intermediate oxidation step on the way toward CO_2 production. In addition, the oxygen storage capacity of the washcoated GPF very nearly ensures that any CO produced will be oxidized to CO_2. Combining all these factors, the CO reaction is ignored in the soot oxidation modeling framework. The oxygen-initiated exothermic soot oxidation reactions are then reduced to only the formation reaction of CO_2:

$$C + O_2 \rightarrow CO_2 \tag{2}$$

3.2. Ceria-initiated soot oxidation reaction kinetics

The presence of ceria provides additional reaction pathways for carbon. Endothermic reactions occupy active ceria (CeO_2) sites in the catalytic coating, while consuming soot particles. This procedure is described by the following chemical reactions (Konstantas & Stamatelos, 2004):

$$\begin{cases} C + 4CeO_2 \rightarrow 2Ce_2O_3 + CO_2 \\ C + 2CeO_2 \rightarrow Ce_2O_3 + CO \end{cases} \quad \textbf{Endothermic} \tag{3}$$

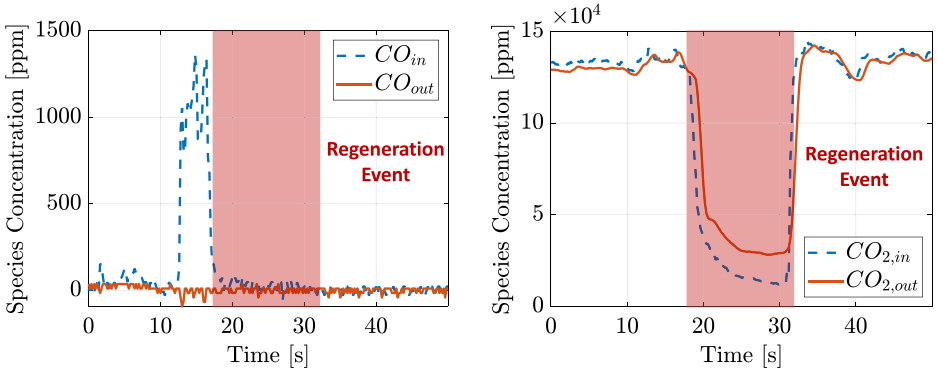

Fig. 3. Experimentally measured pre- and post-GPF ppm of (a) CO_2 and (b) CO gases. The shaded region represents the regeneration event.

Table 1
Enthalpy of reaction values for the three reactions (2), (4), and (5).

Regeneration reaction mechanism	Enthalpy of the reaction
$C + O_2 \rightarrow CO_2$	$\Delta H_T = -393.5$ [kJ/mol]
$2Ce_2O_3 + O_2 \rightarrow 4CeO_2$	$\Delta H_{C,2} = -762.4$ [kJ/mol]
$C + 4CeO_2 \rightarrow 2Ce_2O_3 + CO_2$	$\Delta H_{C,1} = +368.9$ [kJ/mol]

For reasons elaborated in Section 3.1, the reaction which leads to the formation of CO is ignored. This reduces the endothermic ceria-initiated soot oxidation reactions to:

$$C + 4CeO_2 \rightarrow 2Ce_2O_3 + CO_2 \tag{4}$$

Similarly, the exothermic reaction that oxidizes Ce_2O_3 to CeO_2 and generates new free ceria sites is: (Konstantas & Stamatelos, 2004)

$$\left\{ \quad 2Ce_2O_3 + O_2 \rightarrow 4CeO_2 \quad \textbf{Exothermic} \right. \tag{5}$$

Table 1 provides the enthalpy of the three regeneration reactions (2), (4), and (5). The enthalpy of formation values for different chemical reactants and products were obtained from the CRC Handbook of Chemistry and Physics (Lide & Haynes, 2009).

3.3. Formulation of the regeneration reactions

A regeneration event involves the oxidation of trapped soot particles in the presence of an excessive amount of oxygen from the exhaust gas. The regeneration events described in this work are forced by initiating fuel cut-off for a short duration of time, during which the engine switches to a lean operating condition. The internal GPF temperature during this event is typically 300–400°C higher compared to nominal operating conditions due to the exothermic internal reactions.

The volume fraction of the exhaust gas constituents is equal to its molar concentration by assuming ideal gas behavior. As a result, their volume fraction Y_i can be expressed as

$$Y_i = \frac{n_i}{n_{total}} \tag{6}$$

The mathematical expression for the rate of the reaction (2), denoted by R_T, is formulated using the Arrhenius type relationship for the reaction rate constant, denoted by k_T, is then represented as a function of temperature (Atkins et al., 2014):

$$k_T = A_T \cdot \exp\left(-\frac{E_a^T}{RT_{gas}}\right), \tag{7}$$

where A_T and E_a^T represent the pre-exponential factor and activation energy.

The modeling approach in this work considers the GPF as a lumped system with a representative temperature value. The soot particles trapped in the porous walls of the GPF are at the temperature of the ceramic substrate, T_{GPF}.

During tipout, the temperature of the exhaust gas at the GPF inlet starts to drop; however, the temperature inside the GPF starts to rise due to the regeneration reactions that are sustained by the substrate temperature as a result of volumetric heat absorption. As the exhaust gas constituents permeate through the substrate, it is reasonable to assume that the gas temperature is approximately equal to the temperature of the soot particles that it reacts with. The assumption of equal gas and substrate temperatures within the GPF eliminates the need to consider the convection and conduction heat transport that take place between the porous brick and the gas flowing through the pores. Therefore, k_T can be expressed as:

$$k_T = A_T \cdot \exp\left(-\frac{E_a^T}{RT_{GPF}}\right) \tag{8}$$

The reaction rate is directly proportional to the number of moles of the reactant constituents, i.e. the number of moles of carbon, n_C, and the number of moles of oxygen, n_{O_2}. The reaction rate expression for R_T is formulated by normalizing n_{O_2} using n_{total}:

$$\begin{aligned} R_T &= k_T \cdot n_C \cdot \frac{n_{O_2}}{n_{total}} \\ &= A_T \cdot \exp\left(-\frac{E_a^T}{RT_{GPF}}\right) \cdot n_C \cdot \frac{n_{O_2}}{n_{total}} \\ &= A_T \cdot \exp\left(-\frac{E_a^T}{RT_{GPF}}\right) \cdot \frac{m_{c,GPF}}{M_C} \cdot Y_{O_2}, \end{aligned} \tag{9}$$

where n_C is the ratio of the predicted mass of soot, $m_{c,GPF}$, and the molar mass of carbon, M_C. Normalizing n_{O_2} allows the formulation of R_T in terms of Y_{O_2}, and the procedure to determine the volume fraction of the exhaust gas constituents is elaborated in Appendix B.

The reaction rate is expressed in terms of mole fraction and volume fraction. While this is not commonly observed in reaction rate expressions, a similar approach has been implemented for GPF modeling in Boger et al. (2015) and Nicolin et al. (2015) using mass and volume fractions. The rate of the reaction (4), $R_{C,1}$, is mathematically formulated as:

$$R_{C,1} = A_{C,1} \cdot \exp\left(-\frac{E_a^{C,1}}{RT_{GPF}}\right) \cdot \frac{m_{c,GPF}}{M_C} \cdot Z_{CeO_2}, \tag{10}$$

where $A_{C,1}$ and $E_a^{C,1}$ represent the pre-exponential factor and activation energy, and Z_{CeO_2} represents the volume fraction of oxidized ceria. Given that the formation of CeO_2 is an exothermic reaction and the formation of Ce_2O_3 is endothermic, CeO_2 is the more stable compound. As a result, cerium is considered to exist in the washcoat in the form of CeO_2 prior to the initiation of regeneration, and the initial value of Z_{CeO_2} is taken as 0.5.

Finally, the rate of the exothermic reaction (5) that generates active ceria sites is formulated by assuming that the total mass of oxygen that is trapped inside the GPF, m_{O_2}, is available to react with Ce_2O_3. Since cerium exists only in the form of CeO_2 or Ce_2O_3, $Z_{Ce_2O_3}$ is equal to $(1 - Z_{CeO_2})$. Mathematically, the reaction rate is then expressed as:

$$\begin{aligned} R_{C,2} &= A_{C,2} \cdot \exp\left(-\frac{E_a^{C,2}}{RT_{GPF}}\right) \cdot n_{O_2} \cdot Z_{Ce_2O_3} \\ &= A_{C,2} \cdot \exp\left(-\frac{E_a^{C,2}}{RT_{GPF}}\right) \cdot \frac{m_{O_2}}{M_{O_2}} \cdot (1 - Z_{CeO_2}) \\ &= A_{C,2} \cdot \exp\left(-\frac{E_a^{C,2}}{RT_{GPF}}\right) \cdot \frac{\rho_{O_2} Y_{O_2} V_{exh}}{M_{O_2}} \cdot (1 - Z_{CeO_2}), \end{aligned} \tag{11}$$

where the density of oxygen, ρ_{O_2}, is obtained using the ideal gas equation. m_{O_2} is the product of ρ_{O_2} and the overall trapped volume of oxygen in the coated GPF. The latter parameter is the product of the volume fraction of oxygen, Y_{O_2}, and the overall trapped volume of exhaust gases within the coated GPF, V_{exh}.

The oxygen concentrations are derived from wide band lambda sensors, and the volumetric flow of oxygen is then calculated using the vehicles value of exhaust gas mass flow. Even if both inlet and outlet oxygen sensors are utilized in this work, only an inlet sensor is necessary for proper quantification of oxygen entering the GPF.

3.4. Characterization of the thermal dynamics

The thermal energy balance equation is developed by considering different modes of heat transport inside a representative control volume of the GPF, as illustrated in Fig. 4. Energy interactions associated within this control volume are: (i) heat generation from regeneration reactions, (ii) volumetric heat absorption due to the thermal inertia of the ceramic substrate, and (iii) heat carried away by the exhaust gas as they permeate through the GPF. The generalized energy balance equation for the control volume, in rate form, is expressed as (Cengel & Boles, 2002):

$$\begin{aligned} \dot{E}_{CV} = (\dot{Q}_{in} - \dot{Q}_{out}) + (\dot{W}_{in} - \dot{W}_{out}) + (\dot{E}_{mass,in} - \dot{E}_{mass,out}) \\ + \dot{Q}_{int,gen}, \end{aligned} \tag{12}$$

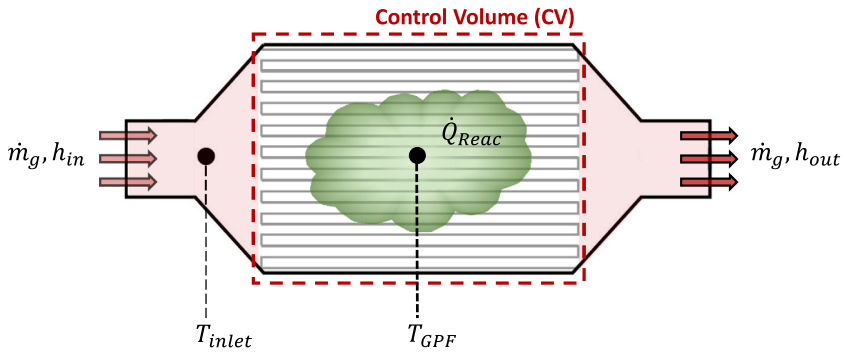

Fig. 4. Schematic representation of the thermal energy balance equation, which involves the rate of heat generation due to reactions, the net rate of change in flow enthalpy of the exhaust gas through the GPF, and the volumetric heat absorption of the ceramic substrate.

where $\dot{E}_{CV}$ represents the rate of net energy transfer in the control volume due to the energy interactions, $\dot{Q}_{in}$ and $\dot{Q}_{out}$ represent heat transfer to and from the control volume, respectively, $\dot{W}_{in}$ and $\dot{W}_{out}$ represent work done on and by the control volume, respectively, $\dot{E}_{mass,in}$ and $\dot{E}_{mass,out}$ represent energy transfer as a result of mass flow in and out of the system, respectively, and $\dot{Q}_{int,gen}$ represents heat generation within the control volume.

Other than the inlet and outlet flow of exhaust gas, there is no heat transport across the boundaries of the control volume. Therefore, $\dot{Q}_{in} = \dot{Q}_{out} = 0$. Moreover, there is no work done on or by the control volume. Hence, $\dot{W}_{in} = \dot{W}_{out} = 0$. $\dot{E}_{mass,in}$ and $\dot{E}_{mass,out}$ result from the transport of the exhaust gas constituents, and are defined as:

$$\begin{aligned} \dot{E}_{mass,in} &= \sum_j (m_{j,in} \cdot h_{j,in}), \quad \text{and} \\ \dot{E}_{mass,out} &= \sum_j (m_{j,out} \cdot h_{j,out}), \end{aligned} \tag{13}$$

where $m_{j,in}$ and $m_{j,out}$ are the mass flow rate of the exhaust gas constituents in and out of the control volume, respectively, while $h_{j,in}$ and $h_{j,out}$ are the specific enthalpy of the exhaust gas constituents in and out of the control volume, respectively. Neglecting any potential and kinetic energy changes in the exhaust gas, and assuming steady flow $(m_{j,in} = m_{j,out} = \dot{m}_g)$,

$$\dot{E}_{mass,in} - \dot{E}_{mass,out} = \dot{m}_g \cdot (h_{gas,in} - h_{gas,out}), \tag{14}$$

where $h_{gas,in}$ and $h_{gas,out}$ represent the specific enthalpies of the exhaust gas entering and leaving the control volume, respectively. The heat of a reaction is equal to the product of the reaction rate and the reaction enthalpy of formation. The net amount of heat generated due to the regeneration reactions (2), (4), and (5) is:

$$\dot{Q}_{Reac} = (-\Delta H_T) \cdot R_T + (-\Delta H_{C,1}) \cdot R_{C,1} + (-\Delta H_{C,2}) \cdot R_{C,2} \tag{15}$$

$(-\Delta H_T) \cdot R_T$ and $(-\Delta H_{C,2}) \cdot R_{C,2}$ are the exothermic heat of the reactions (2) and (5) respectively, while $(-\Delta H_{C,1}) \cdot R_{C,1}$ is the endothermic heat of reaction (4). Since the only source of heat generation within the control volume is due to the regeneration reactions, $\dot{Q}_{int,gen} = \dot{Q}_{Reac}$. Therefore, (12) reduces to:

$$\dot{E}_{CV} = \dot{m}_g \cdot (h_{gas,in} - h_{gas,out}) + \dot{Q}_{Reac} \tag{16}$$

Assuming that the exhaust gas constituents exhibit ideal gas behavior, the difference in the specific enthalpies is equal to (Cengel & Boles, 2002):

$$h_{gas,in} - h_{gas,out} = (e_{gas,in} - e_{gas,out}) + R_{gas}(T_{inlet} - T_{outlet}), \tag{17}$$

where $e_{gas,in}$ and $e_{gas,out}$ represent the internal energy of the exhaust gas entering and leaving the control volume, respectively, R_{gas} is the specific gas constant, and T_{inlet} and T_{outlet} are the temperature of the gas entering and leaving the control volume, respectively. Assuming that the gas composition entering and leaving the control volume is the same, the difference in the specific enthalpies can be reformulated as (Cengel & Boles, 2002):

$$\begin{aligned} &h_{gas,in} - h_{gas,out} \\ &= C_{v,gas} \cdot (T_{inlet} - T_{outlet}) + R_{gas} \cdot (T_{inlet} - T_{outlet}) \\ &= (C_{v,gas} + R_{gas}) \cdot (T_{inlet} - T_{outlet}) \\ &= C_{p,gas} \cdot (T_{inlet} - T_{outlet}), \end{aligned} \tag{18}$$

where $C_{v,gas}$ and $C_{p,gas}$ represent the exhaust gas specific heat capacity at constant volume and constant pressure, respectively.

For model development purposes, it is assumed in this work that T_{outlet} is approximately equal to the temperature of the gas within the GPF, T_{GPF}. This assumption can be made if heat transfer to the exhaust gas within the GPF channels and wall pores is assumed to be fast relative to the mass transport of exhaust gas through the GPF.[1] In general, the temperature of the exhaust gas inside the GPF is expected to be higher than the temperature of the exhaust gas at the GPF outlet. Any physical discrepancy in the numerical values generated by the assumption $T_{outlet} \cong T_{GPF}$ is accounted for by the identified value of the specific heat of the cordierite in the GPF, $C_{p,cord}$, using data from experiments conducted under transient operating conditions. This identification study is elaborated in Section 4.2.

The ceramic substrate within the control volume can be treated as a stationary system which does not undergo any change in velocity or elevation. As a result, changes in the kinetic and potential energies of the substrate are zero. Therefore, the change in the energy inside the control volume with respect to time is equal to the volumetric heat absorption of the substrate:

$$\dot{E}_{CV} = m_{GPF} \cdot C_{p,cord} \cdot \frac{dT_{GPF}}{dt}, \tag{19}$$

where m_{GPF} is the product of the density of cordierite, ρ_{GPF}, and the total cordierite volume, V_{cord}. Finally, the thermal energy balance equation can be summarized as:

$$m_{GPF} \cdot C_{p,cord} \cdot \frac{dT_{GPF}}{dt} = \dot{m}_g \cdot C_{p,gas} \cdot (T_{inlet} - T_{GPF}) + \dot{Q}_{Reac} \tag{20}$$

In this model, $C_{p,gas}$ is a function of T_{inlet} and the determination of this parameter is elaborated in Appendix B.

3.5. Characterization of the soot oxidation dynamics

The oxidation dynamics of soot mass trapped inside the GPF is modeled by assuming uniform deposition and concentration inside the device (Nicolin et al., 2015). The exothermic reactions (2) and (4) are

[1] This assumption is especially relevant for low mass flow conditions, such as regeneration through a throttle tip-out, which is a condition of specific interest for this study as the low exhaust mass flow results in the highest observed GPF temperatures and the greatest risk for GPF health.

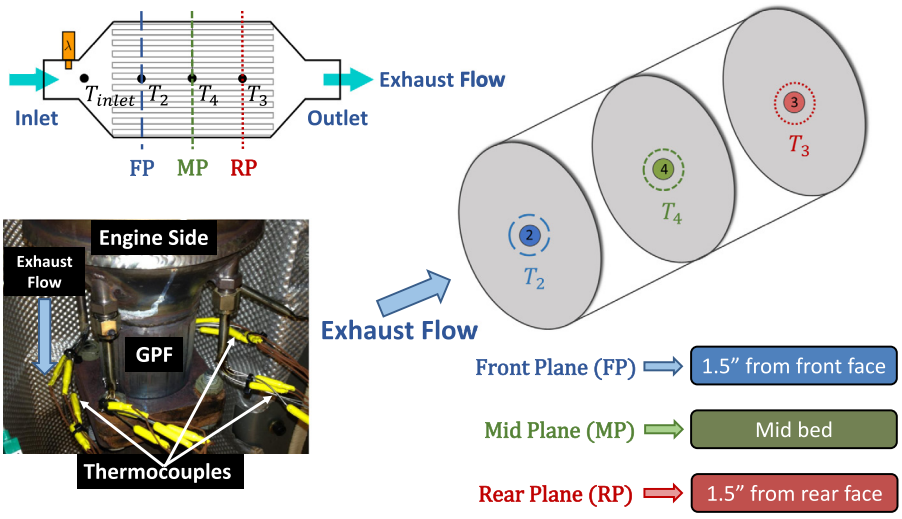

Fig. 5. Schematic representation of the location of different thermocouples to measure the internal GPF temperature.

collectively responsible for the decrease in soot mass during regeneration events. As a result, the time rate of change of soot moles is equal to the sum of the exothermic reaction rates:

$$\frac{dn_C}{dt} = (R_T + R_{C,1}) \tag{21}$$

This expression can be reformulated to express the soot mass rate of change as:

$$\begin{aligned}\frac{dm_{c,GPF}}{dt} &= -M_C \cdot (R_T + R_{C,1}) \\ &= -A_T \cdot \exp\left(-\frac{E_a^T}{RT_{GPF}}\right) \cdot m_{c,GPF} \cdot Y_{O_2} \\ &\quad - A_{C,1} \cdot \exp\left(-\frac{E_a^{C,1}}{RT_{GPF}}\right) \cdot m_{c,GPF} \cdot Z_{CeO_2}\end{aligned} \tag{22}$$

To calculate the amount of soot oxidized during regeneration, it is necessary to model the formation and consumption of available ceria sites for carbon interaction. Since the volume fractions of CeO_2 and Ce_2O_3 are related, the variation of Z_{CeO_2} with time has been used to represent the dynamics of ceria sites in the coated GPF. Reaction (4) is responsible for the creation of active sites while reaction (5) is responsible for the consumption of active sites. Therefore, the net generation of active ceria sites is defined by the difference in the rates of the endothermic and exothermic reactions. Since Z_{CeO_2} is a normalized quantity, $(M_C/m_{c,init})$ and $M_{O_2}/(\rho_{O_2} \cdot V_{exh})$ have been chosen as normalizing factors for the reaction rates $R_{C,1}$ and $R_{C,2}$, respectively, to ensure dimensional consistency. $m_{c,init}$ represents the initial mass of soot prior to regeneration. The dynamic equation for Z_{CeO_2} is then expressed as:

$$\begin{aligned}\frac{dZ_{CeO_2}}{dt} &= -R_{C,1} \cdot \left(\frac{M_C}{m_{c,init}}\right) + R_{C,2} \cdot \left(\frac{M_{O_2}}{\rho_{O_2} \cdot V_{exh}}\right) \\ &= -A_{C,1} \cdot \exp\left(-\frac{E_a^{C,1}}{RT_{GPF}}\right) \cdot \frac{m_{c,GPF}}{m_{c,init}} \cdot Z_{CeO_2} \\ &\quad + A_{C,2} \cdot \exp\left(-\frac{E_a^{C,2}}{RT_{GPF}}\right) \cdot Y_{O_2} \cdot (1 - Z_{CeO_2})\end{aligned} \tag{23}$$

4. Determination of the model parameters

This section begins with a description of the experimental characterization of the ceria-coated GPF, followed by the identification studies for the determination of the specific heat capacity of the cordierite, $C_{p,cord}$, and the pre-exponential factor and activation energy parameters associated with the regeneration reactions (2), (4), and (5). These identification studies are conducted using the Matlab implementation of the particle swarm optimization (PSO)[2] algorithm (Ebbesen, Kiwitz, & Guzzella, 2012).

Table 2
Overview of the parameters of the coated GPF model. Using information from T_{inlet}, λ, and ρ_{soot}, the model predicts T_{GPF} and $m_{c,GPF}$. R, M_C, and M_{O_2} are universal parameters with designated values.

Equation	Model parameters
$R_T = A_T \cdot \exp\left(-\frac{E_a^T}{RT_{GPF}}\right) \cdot \frac{m_{c,GPF}}{M_C} \cdot Y_{O_2}$	$[A_T, E_a^T, Y_{O_2}]$
$R_{C,1} = A_{C,1} \cdot \exp\left(-\frac{E_a^{C,1}}{RT_{GPF}}\right) \cdot \frac{m_{c,GPF}}{M_C} \cdot Z_{CeO_2}$	$[A_{C,1}, E_a^{C,1}, Z_{CeO_2}]$
$R_{C,2} = A_{C,2} \cdot \exp\left(-\frac{E_a^{C,2}}{RT_{GPF}}\right) \cdot \frac{\rho_{O_2} Y_{O_2} V_{exh}}{M_{O_2}} \cdot (1 - Z_{CeO_2})$	$[A_{C,2}, E_a^{C,2}, \rho_{O_2}, V_{exh}]$
$\dot{Q}_{Reac} = (-\Delta H_T) \cdot R_T + (-\Delta H_{C,1}) \cdot R_{C,1} + (-\Delta H_{C,2}) \cdot R_{C,2}$	$[\Delta H_T, \Delta H_{C,1}, \Delta H_{C,2}]$
$m_{GPF} \cdot C_{p,cord} \cdot \frac{dT_{GPF}}{dt} = \dot{m}_g \cdot C_{p,gas} \cdot (T_{inlet} - T_{GPF}) + \dot{Q}_{Reac}$	$[\rho_{GPF}, V_{cord}, C_{p,cord}, C_{p,gas}]$

Table 2 summarizes the different parameters of the model. Appendix A summarizes the determination of the volumetric model parameters V_{cord} and V_{exh}. Appendix B elaborates upon the determination of the exhaust gas parameters Y_i, ρ_{O_2}, and $C_{p,gas}$, where i represents the constituent gases N_2, O_2, CO_2, and H_2O. Appendix C outlines the approach to calculate the total amount of soot oxidized during a regeneration event, $m_{c,exp}$. The methodology to determine the remaining model parameters is presented in this section.

4.1. Experimental characterization of a ceria-coated GPF

Experimental work, data acquisition, and data analysis associated with the soot accumulation and soot regeneration stages were conducted at the Chassis Dynamometer laboratory located at the Clemson University International Center for Automotive Research.[3] A comprehensive description of this experimental work has been presented in Rathod, Onori, Filipi, and Hoffman (2018). Experimental data sets were developed with different initial soot loading and temperatures at the onset of regeneration. For each data set, multiple regeneration

[2] PSO is a non-gradient based evolutionary computational approach, designed by observing the social behavior of certain animal species, to achieve the global minimum for a fitness function by moving a population of possible solutions, constituting the *swarm*, through a multi-dimensional solution hyperspace in an iterative manner.

[3] The authors of this manuscript were affiliated with the Department of Automotive Engineering, Clemson University, Greenville, SC 29607, USA, when the experimental work and model development studies were undertaken.

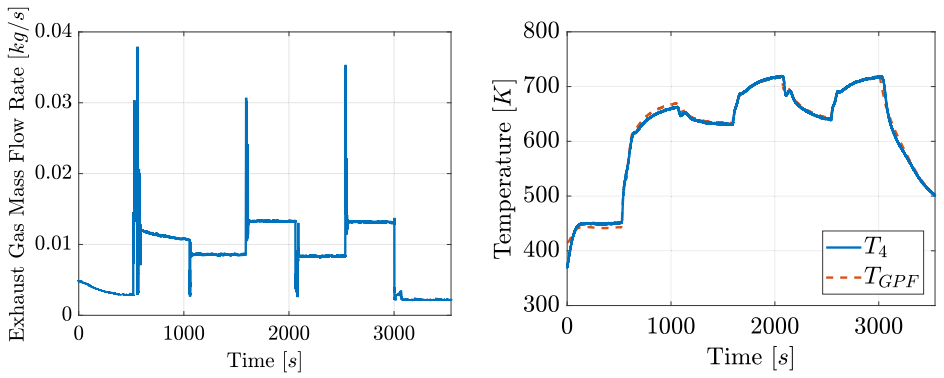

Fig. 6. (a) Exhaust gas mass flow rate as calculated in the engine control unit, and (b) comparison of T_{GPF} and T_4 during the identification study to determine the parameter $C_{p,cord}$. This identification study is elaborated in Section 4.2.

events were performed in a sequential manner to gradually decrease the overall amount of soot accumulated in the coated GPF through oxidation.

Temperature measurements were obtained by installing K-type thermocouples in the GPF according to the layout shown in Fig. 5. Sensor locations 2, 3, and 4 represent the GPF internal temperatures along the flow centerline of the front-plane, rear-plane, and mid-plane, respectively.

The pre- and post-GPF ppm levels of CO and CO_2 gases were measured by simultaneously passing the respective gas streams through a dual channel Fourier Transform Infrared Spectroscopy (FTIR) analyzer with equivalent sample line lengths and sample flow rates.

Prior to regeneration, the engine is switched to lean operation, producing a precipitous decrease in CO_2 pre-GPF. Because of the presence of a TWC upstream of the GPF, the decline in CO_2 concentration is gradually observed, instead of a step change as seen in the measured exhaust gas mass flow rate, $\dot{m}_g$. Due to the presence of a higher amount of O_2 inside the GPF compared to nominal operation, the post-GPF CO_2 levels increase beyond the inlet, indicating regeneration. During the onset of regeneration, the air–fuel ratio λ, measured using a wide range lambda sensor mounted upstream of the GPF, is greater than the stoichiometric value of 1. When the regeneration event is terminated, the post-TWC air–fuel ratio returns to its stoichiometric value.

Prior to regeneration, soot accumulation experiments were performed with the coated GPF installed downstream of a TWC on a vehicle operating at a constant engine load for extended periods of time. Based on the engine operating conditions and $\dot{m}_g$, the backpressure developing across the GPF (measured using a differential pressure sensor) and soot mass accumulation were determined. Accumulation experiments were specifically designed to produce different initial soot loading densities within the coated GPF.

The GPF inlet temperature at the onset of each successive regeneration event was increased to enhance the soot oxidation reaction kinetics despite the decreasing GPF carbon concentration after each successive regeneration event. Note that utilizing a conservative inlet temperature at the onset of the first regeneration minimizes the risk of overheating the GPF during soot oxidation. For every experimental regeneration event, it is possible to determine the initial and final soot mass inside the coated GPF from the pre- and post-GPF CO_2 ppm measurements. This is outlined in Appendix C.

4.2. Identification of $C_{p,cord}$

A *clean* experimental data set prior to any soot accumulation was used to identify $C_{p,cord}$. The objective of this parameter identification study is to determine the value of $C_{p,cord}$ such that the model-predicted temperature T_{GPF} matches the experimental measurement T_4 as accurately as possible. Mathematically, this is defined using a thermal-based cost function, J:

$$J = \sqrt{\frac{1}{N}\sum_{i=1}^{N}\left(T_4(i) - T_{GPF}(i)\right)^2} \cdot \frac{100}{\max(T_4)}\ , \tag{24}$$

where N is the total number of data samples and i is the time index.[4] Because the underlying equations constitute a lumped parameter model, it is assumed that the wall and gas temperatures inside the GPF are equal, due to the permeation of the gas through the substrate. Since the experimental data set used for identification does not contain any regeneration events, the reaction rates R_T, $R_{C,1}$, and $R_{C,2}$ are equal to zero. As a result, the thermal dynamic equation inside the coated GPF reduces to:

$$\begin{aligned}&\rho_{GPF} \cdot V_{cord} \cdot C_{p,cord} \cdot \frac{dT_{GPF}}{dt} \\ &= -\dot{m}_g \cdot C_{p,gas} \cdot (T_{GPF} - T_{inlet})\end{aligned} \tag{25}$$

The dynamic variation of $\dot{m}_g$ during the experiment is illustrated in Fig. 6(a). The result of this identification study is schematically represented in Fig. 6(b). The RMS error obtained during this identification study is 0.88%, and the identified value of the parameter $C_{p,cord}$ is 1173.3 [J/(kg · K)].

4.3. Identification of the remaining model parameters

In Arunachalam et al. (2017), the lumped thermal dynamics in a ceria-coated GPF were characterized using a set of 11 parameters, identified using experimental data, with the vector of identified parameters, θ_{ini}, being:

$$\begin{aligned}\theta_{ini} = \big[&A_T\ A_{C,1}\ A_{C,2}\ E_a^T\ E_a^{C,1}\ E_a^{C,2} \\ &\Delta H_T\ \Delta H_{C,1}\ \Delta H_{C,2}\ C_{p,cord}\ C_{p,gas}\big]^T\end{aligned} \tag{26}$$

In this work, the identification approach was improved and the vector of identified parameters was reduced to θ, defined as:

$$\theta = \left[A_T\ A_{C,1}\ A_{C,2}\ \ E_a^{C,1}\ E_a^{C,2}\right]^T \tag{27}$$

This reduction of the number of elements in the vector θ was achieved due to the following factors:

[4] Experimental measurements revealed an insignificant difference in the internal GPF temperature at locations 2, 3, and 4. Therefore, T_4 was chosen instead of T_{avg} as it represented the central axial location of the GPF. Replacing T_{avg} with T_4 is not expected to affect the outcome of this identification study.

Table 3
T_{inlet} at the onset of regeneration, and the amount of soot oxidized during each of the regeneration events for the two data sets.

Experimental data set	Soot loading density	Regeneration event	Initiation temperature	Amount of soot oxidized
I	2.00 [g/l]	First regeneration event (Regen 1a)	670 °C	0.2360 [g]
		Second regeneration event (Regen 2a)	700 °C	0.2654 [g]
		Third regeneration event (Regen 3a)	750 °C	1.2050 [g]
		Fourth regeneration event (Regen 4a)	775 °C	1.0750 [g]
II	0.67 [g/l]	First regeneration event (Regen 1b)	700 °C	0.3063 [g]
		Second regeneration event (Regen 2b)	700 °C	0.1672 [g]
		Third regeneration event (Regen 3b)	750 °C	0.4550 [g]

1. Sensitivity analysis studies indicated that the model-predicted response is strongly influenced by small variations in the parameter E_a^T. Nicolin et al. (2015) performed isothermal thermogravimetric analysis experiments and determined E_a^T to be equal to 150 [kJ/mol]. The results from sensitivity analysis revealed that an E_a^T value of 149 [kJ/mol] predicts temperature and soot oxidation dynamics with reasonable accuracy.
2. ΔH_T, $\Delta H_{C,1}$, and $\Delta H_{C,2}$ were determined using thermochemical tables, and are summarized in Table 1.
3. $C_{p,cord}$ was determined with a dedicated experimental data set prior to soot accumulation in the GPF and using the method outlined in Section 4.2.
4. $C_{p,gas}$ is dependent on temperature and volume fraction of the exhaust gas constituents. The determination of this parameter is presented in Appendix B.

The lumped parameter model proposed in Section 3 utilizes experimental measurements of the exhaust gas temperature at the GPF inlet and the mass air flow rate of the exhaust gas as input parameters. Parameter identification is performed by considering the regeneration events that occur within the coated filter.

4.3.1. Experimental data used for parameter identification

Two experimental data sets, characterized by different initial soot loading density (SLD) values, were used for the identification study. Since soot oxidation dynamics vary spatially within the coated GPF, the average of T_2, T_3, and T_4 was chosen as a characteristic representation of the internal GPF temperature, and denoted by T_{avg}. This selection is justified due to the strategic location of these 3 thermocouples along the axial direction of the GPF, combined with the argument that the lumped parameter model considers uniform behavior across the GPF.

Table 3 summarizes the regeneration events in each data set, along with T_{inlet} at the onset of regeneration and the amount of soot oxidized during each event. Figs. C.17 (b) and C.19 represent the variation in pre- and post-GPF CO_2 ppm levels during Regen 1a and the amount of soot oxidized, respectively. SLD is obtained by dividing the total amount of soot oxidized in all the regeneration events of a data set with the volume of the coated GPF, V_{filter}. The value of the SLD for experimental data set I is:

$$\text{SLD}_{\text{I}} = \frac{\sum_{i=1}^{F} m_{c,regen}(i)}{V_{filter}} = \frac{0.2360 + 0.2654 + 1.2050 + 1.0750}{1.39} = 2.00 \text{ [g/l]}. \tag{28}$$

i refers to a particular regeneration event, F is the number of regeneration events in a data set, and $m_{c,regen}(i)$ is the amount of soot oxidized in [g] during event i. Similarly, SLD_{II} is calculated to be 0.67 [g/l]. Henceforth, experimental data sets I and II will be referred to as 2.00 [g/l] and 0.67 [g/l] data sets, respectively.

4.3.2. Cost function for the parameter identification study

A *combined* cost function, with equal weights, was designed that simultaneously minimizes the error between the experimental and model-predicted thermal and soot oxidation dynamics. Additionally, two other cost functions, *thermal* and *soot*, were also investigated for the prediction of the thermal and soot oxidation dynamics, respectively. The results from the latter identification study using these two cost functions are presented in Appendix D.

Table 4
Setup of the parameter identification study.

PSO option	Value/Setting
options.SwarmSize	50000
options.MaxIter	100
options.TolFun	0.5×10^{-6}
options.StallIterLimit	10
options.InertialRange	[0.1, 1.1]
options.SelfAdjustmentWeight	1.49
options.SocialAdjustmentWeight	1.49

Table 5
The range of variation of the parameters during identification.

Parameter	Identification range
A_T	$[1 \times 10^5,\ 1 \times 10^8]$
$A_{C,1}$	$[1 \times 10^7,\ 1 \times 10^{10}]$
$A_{C,2}$	$[1 \times 10^7,\ 1 \times 10^{10}]$
$E_a^{C,1}$	$[1 \times 10^6,\ 1 \times 10^8]$
$E_a^{C,2}$	$[1 \times 10^4,\ 1 \times 10^7]$

The parameters in the vector θ, given in (27), are identified using the PSO algorithm and minimizing the *combined* cost function, J_C:

$$J_C(\theta) = \left\{ \frac{1}{N} \sum_{i=1}^{N} \left(\frac{T_{avg}(i) - T_{GPF}(\theta; i)}{\max(T_{avg})} \right)^2 + \frac{1}{N} \sum_{i=1}^{N} \left(\frac{m_{c,exp}(i) - m_{c,GPF}(\theta; i)}{\max(m_{c,exp})} \right)^2 \right\}^{0.5} \tag{29}$$

T_{GPF} is the model-predicted temperature that is a function of θ, $m_{c,exp}$ is the experimentally determined mass of soot oxidized during a regeneration event, and $m_{c,GPF}$ is its corresponding model-predicted value which is a function of θ.

4.3.3. Details of the parameter identification study

Table 4 summarizes the setup of the parameter identification study. The termination criteria was defined as either 100 completed generations *or* the completion of 10 successive generations without any improvement in the cost function. Table 5 lists the identification range for the elements of the parameter vector θ. The identification range for the pre-exponential factors and the activation energies have been developed based on the work of Konstantas and Stamatelos (2004). The selected identification range considers the loss in physical meaning of the proposed control-oriented model parameters due to the omission of GPF transport dynamics.

4.3.4. Modification of $\dot{m}_g$ and T_{inlet}

In order to maintain stoichiometric air–fuel ratio during nominal operation, $\dot{m}_g$ is determined by the engine control unit prior to the

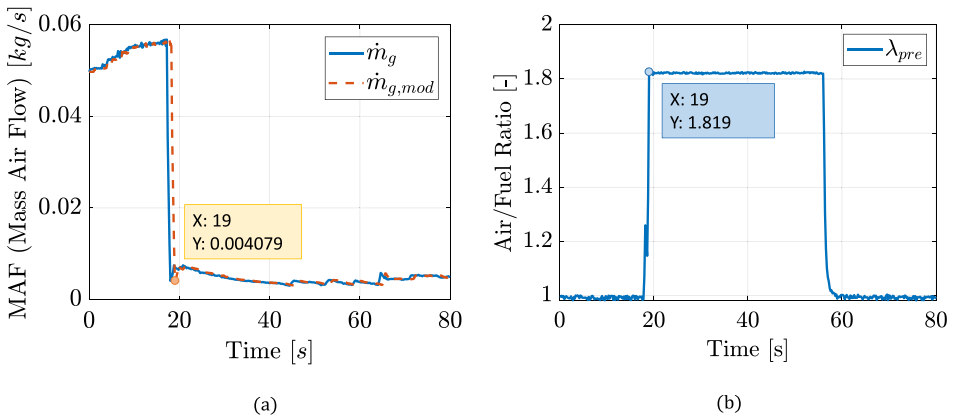

Fig. 7. (a) The original and modified mass air flow of exhaust gas, and (b) the measured pre-GPF air fuel ratio.

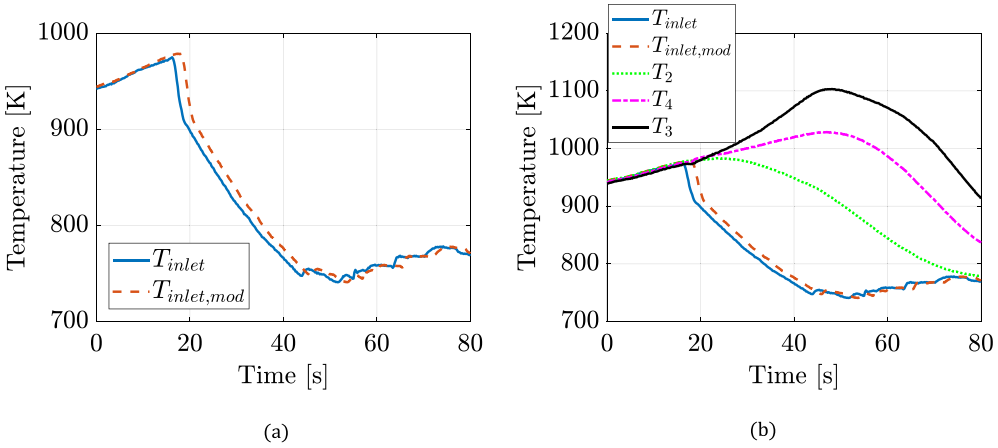

Fig. 8. (a) The original and modified GPF inlet exhaust gas temperature, and (b) comparison of the GPF inlet exhaust gas temperature with the other measured GPF internal temperatures.

induction of air into the combustion chamber. The mass of air flowing into the intake manifold is measured using a hot wire anemometer. Because of physical transport delays associated with exhaust gas transport to the GPF, $\dot{m}_g$ must be estimated at the inlet of the GPF.

In order for the dynamic change in $\dot{m}_g$ to accurately reflect the onset of a regeneration event, $\dot{m}_g$ is adjusted with respect to the pre-GPF air–fuel ratio, λ_{pre}. Fig. 7 illustrates the modification to $\dot{m}_g$ for the Regen 1b data set. The original $\dot{m}_g$ is shifted by 0.8 s to the right such that the rapid decline in $\dot{m}_g$ coincides with the rapid rise in λ_{pre} during the initiation of regeneration. When λ_{pre} reaches its saturation limit, the modified mass air flow $\dot{m}_{g,mod}$ reaches it lowest point during the decline.

In addition, it was observed from the experimentally acquired data that T_{inlet} was lower than the temperatures T_2, T_3, and T_4 prior to the onset of regeneration. During nominal operation, the internal GPF temperatures are expected to be lower than T_{inlet} due to the volumetric heat absorption of the GPF ceramic substrate. This anomaly in the measurement of T_{inlet} was rectified by considering the value of T_{inlet} before the initiation of regeneration to be equal to that of T_2, the sensor that is located nearest to the thermocouple measuring T_{inlet}.

Fig. 8 illustrates the modification to T_{inlet} for the Regen 1b data set. Until the onset of regeneration, the modified GPF inlet exhaust gas temperature $T_{inlet,mod}$ is equal to T_2. Once the regeneration event begins, $T_{inlet,mod}$ is equal to the value of T_{inlet} during the decline in temperature. Similar modifications were made for $\dot{m}_g$ and T_{inlet} for all the other data sets used for parameter identification and model validation.

4.3.5. Results of the parameter identification study

This section presents the parameter identification results using the *combined* cost function for the Regen 2b experimental data set. The results for this event have been selected for presentation as it is centrally positioned with regards to the three regeneration event soot loadings. The initial and final amount of soot inside the coated GPF is known, and is different from $\sum_{i=1}^{F} m_{c,regen}(i)$ or 0. Parameter identification for all the other regeneration events is performed in the same manner.

For each experimental data set, it is assumed that the GPF was completely purged of all soot prior to the soot accumulation experiments. As a result, at the end of the accumulation experiment, the total amount of soot mass inside the coated GPF is equal to $\sum_{i=1}^{F} m_{c,regen}(i)$. Another critical assumption is that soot accumulation and soot oxidation during nominal vehicle operation (when there are no forced regeneration events) is negligible. This assumption is reasonable due to the location of the GPF downstream of a functional TWC and the operation of the vehicle's closed loop lambda control.

For the 0.67 [g/l] data set, the total amount of initial soot mass is calculated based on the values provided in Table 3, and is equal to 0.9285 [g]. At the end of Regen 1b, 0.3063 [g] of soot has been lost to oxidation. Therefore, the amount of soot remaining in the GPF is the difference between these values, and is equal to 0.6277 [g]. This is also the value of the soot mass at the beginning of Regen 2b. During Regen 2b, the amount of soot oxidized is 0.1672 [g]. Hence, the amount of soot inside the coated GPF after Regen 1b and Regen 2b is 0.4550 [g].

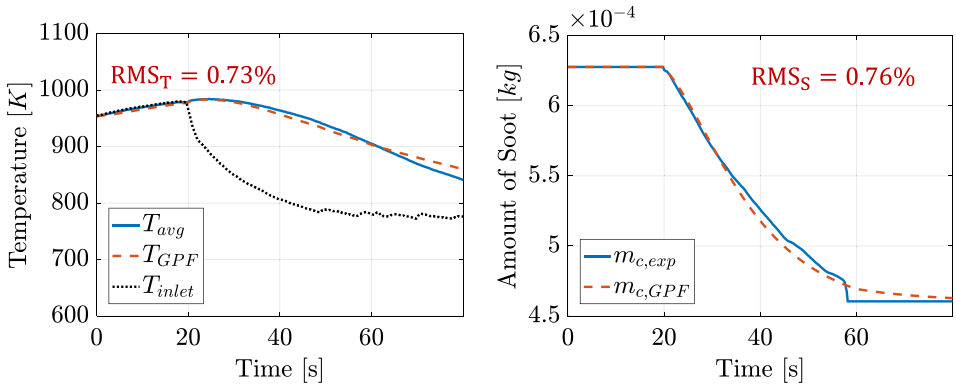

Fig. 9. Identification results using the combined cost function to evaluate the (a) thermal and (b) soot oxidation response of the model.

Table 6
Summary of the approaches outlined in this work to determine the different parameters of the proposed model.

Model parameters	Determination approach	Reference
ΔH_T, $\Delta H_{C,1}$, and $\Delta H_{C,2}$	Calculated using the enthalpies of formation of reaction species	Section 3.2
$C_{p,cord}$	Obtained from parameter identification using a *clean* experimental data set	Section 4.2
E_a^T	Set to a value of 149 [kJ/mol] based on sensitivity analysis studies	Section 4.3
A_T, $A_{C,1}$, $A_{C,2}$, $E_a^{C,1}$, and $E_a^{C,2}$	Obtained from the parameter identification studies	Section 4.3
V_{cord} and V_{exh}	Calculated using geometric information	Appendix A
Y_{O_2}, ρ_{O_2}, and $C_{p,gas}$	Calculated using experimental data	Appendix B

Table 7
Identified values of the elements of the vector θ using the *combined* cost function.

Data set	A_T	$A_{C,1}$	$A_{C,2}$	$E_a^{C,1}$	$E_a^{C,2}$	Input parameter values
Regen 1a	0.20*e*7	1.97*e*9	1.49*e*9	0.67*e*6	1.76*e*5	$m_{c,init}$ = 2.78 [g] and T_{init} = 949.5 [K]
Regen 2a	0.20*e*7	1.97*e*9	1.49*e*9	0.67*e*6	1.76*e*5	$m_{c,init}$ = 2.54 [g] and T_{init} = 949.6 [K]
Regen 1b	0.44*e*7	6.48*e*9	2.44*e*9	0.72*e*6	1.84*e*5	$m_{c,init}$ = 0.93 [g] and T_{init} = 959 [K]
Regen 2b	0.25*e*7	0.06*e*9	9.67*e*9	0.18*e*6	1.97*e*5	$m_{c,init}$ = 0.63 [g] and T_{init} = 972 [K]
Regen 3b	1.17*e*7	9.69*e*9	9.77*e*9	1.00*e*6	7.12*e*5	$m_{c,init}$ = 0.46 [g] and T_{init} = 1022 [K]

The % Root Mean Square (RMS) error between the experimental and the model-predicted thermal response is:

$$\mathrm{RMS_T} = \sqrt{\frac{1}{N}\sum_{i=1}^{N}\left(T_{avg}(i) - T_{GPF}(\theta;i)\right)^2} \cdot \frac{100}{\max(T_{avg})} \tag{30}$$

Similarly, the % RMS error between the experimental and the model-predicted amount of soot oxidized is obtained with:

$$\mathrm{RMS_S} = \sqrt{\frac{1}{N}\sum_{i=1}^{N}\left(m_{c,exp}(i) - m_{c,GPF}(\theta;i)\right)^2} \cdot \frac{100}{\max(m_{c,exp})} \tag{31}$$

Fig. 9 presents parameter identification results using the *combined* cost function. Equal weighting factors are utilized on the thermal and soot errors to predict the response of the model for thermal and soot oxidation dynamics. The RMS$_T$ and RMS$_S$ values obtained from this identification are respectively 0.73% and 0.76%. Based on the results of the identification study, the *combined* cost function provides a satisfactory response for the model-predicted thermal and soot oxidation dynamics. Moreover, to reduce the computational burden and make the identification process more effective, the same set of parameters is identified for Regen 1a and 2a (Table 7). This is a reasonable simplification since, for the aforementioned experiments, the GPF temperatures T_{init} are practically the same. For model validation, the parameters that have been identified using this cost function have been utilized.

5. Model validation results and their implications

Table 6 summarizes the sequence of operations to determine the different model parameters. Table 7 summarizes the identified values of the model parameters using the *combined* cost function for five regeneration events for the 2.00 [g/l] and 0.67 [g/l] data sets.

The elements of the vector θ are a function of the initial soot mass prior to regeneration, $m_{c,init}$, and T_{inlet}. For each regeneration event, the value of T_{inlet} at the beginning of regeneration, hereafter denoted by T_{init}, is used as the input. More precisely, T_{init} is the value of T_{inlet} at the exact time instant when the air–fuel ratio sensor saturates at its maximum value of ≈ 1.8 for the very first time before the initiation of regeneration.

The proposed model is implemented in Matlab Simulink®, and the results presented in this paper are based on a 1-D look-up table that utilizes the values of T_{init}.

For model validation, an experimental data set with an initial SLD value of 1.16 [g/l] has been used. This data set, hereafter represented as soot loading 'c', was selected because the initial SLD value lies between the initial SLD values utilized for parameter identification. Table 8 summarizes the different regeneration events for the 1.16 [g/l] data set, along with the amount of soot oxidized during each event. The results of model validation for regeneration events Regen 1c and Regen 2c are presented in Table 9 for two T_{init} values of the two validation data sets, and the interpolated values of the elements of the vector θ obtained using the 1-D thermal look-up table.

Table 8
T_{inlet} at the onset of regeneration, and the amount of soot oxidized during each regeneration event in the 1.16 [g/l] experimental data set.

Experimental data set	Regeneration event	Initiation temperature	Amount of soot oxidized
1.16 [g/l]	First regeneration event (Regen 1c)	670 °C	0.4938 [g]
	Second regeneration event (Regen 2c)	700 °C	0.2264 [g]
	Third regeneration event (Regen 3c)	750 °C	0.6185 [g]
	Fourth regeneration event (Regen 4c)	775 °C	0.2707 [g]

Table 9
Interpolated values of the elements of the vector θ, based on a 1-D look-up table that utilized the value of T_{init}.

Data set	A_T	$A_{C,1}$	$A_{C,2}$	$E_a^{C,1}$	$E_a^{C,2}$	Input parameter values
Regen 1c	3.58e6	3.67e9	5.60e9	4.84e5	1.90e5	T_{init} = 964.7 [K]
Regen 2c	3.50e6	3.38e9	5.94e9	4.59e5	1.90e5	T_{init} = 965.3 [K]

Table 10
Error in the prediction of the amount of soot inside the GPF post each regeneration event.

Data set	Value of $(m_{c,exp} - m_{c,GPF})$ at the end of the regeneration event
Regen 1a	−0.047 [g]
Regen 1b	−0.061 [g]
Regen 2a	−0.092 [g]
Regen 2b	−0.023 [g]
Regen 2c	−0.074 [g]
Regen 1c	−0.033 [g]
Regen 2c	0.087 [g]

For Regen 1c, the pre- and post-regeneration soot mass inside the coated GPF are respectively 1.6094 [g] and 1.1156 [g]. Fig. 10 represents the model performance for thermal and soot oxidation dynamics during Regen 1c. The RMS_T and RMS_S values are respectively 4.32% and 1.73%. For Regen 2c, the pre- and post-regeneration soot mass inside the coated GPF are respectively 1.1156 [g] and 0.8892 [g]. Fig. 11 represents the model performance for thermal and soot oxidation dynamics during Regen 2c. The RMS_T and RMS_S values are respectively 0.90% and 6.31%.

The results indicate that the model-predicted thermal dynamics is within an RMS error of 5% in comparison with T_{avg}. The relatively large value of RMS_S may be attributed to the utilization of only T_{init} for the interpolated parameter values. One approach to address this issue is to conduct more regeneration events and enhance the 1-D temperature-based look-up table through different sets of identified parameter values. Table 10 summarizes the error in the difference in the amount of soot at the end of regeneration for all the data sets presented in this work.

The implementation of a lumped parameter model is challenging due to the lack of a physical reference for characterization. Since internal GPF dynamics are neglected, the model assumes an even dispersion of soot throughout the filter and a single filter temperature. It is not reasonable to expect that the lumped model incorporate the heat generation at different GPF locations and provide a thermal response accordingly. This is the reason behind the selection of an averaged experimental temperature T_{avg} for the parameter identification study presented in Section 4.3.

In reality, the response of the internal GPF temperature sensors is greatly influenced by localized heat generation from soot reactions in other internal locations either by convection due to exhaust gas transport, or by conduction through the cordierite.

The model validation results presented in this section have the following implications, namely:

1. The proposed model eliminates the need for expensive and impractical internal GPF temperature sensors to monitor its performance during accumulation and regeneration events. As a result, maintenance requirements and the need for data acquisition devices associated with such sensors can be avoided.
2. High temperatures are detrimental to the health of the GPF washcoat and the cordierite substrate. Prolonged exposure to aggressive thermal conditions may result in performance deterioration and material disintegration (Nicolin et al., 2015). The proposed model is capable of addressing this critical issue. Model-based OBD strategies can be developed to control the GPF temperature and regeneration duration.

6. Conclusions

This paper presents a control-oriented model to predict the thermal and soot oxidation dynamics in a ceria-coated GPF during nominal operation and regeneration events. The model incorporates oxygen-initiated and catalytic ceria-initiated soot oxidation reactions to determine the internal GPF temperature and the mass of soot oxidized during a regeneration event. The thermal dynamics of the model are characterized by considering reactive heat generation, the thermal inertia of the GPF cordierite, and net heat transfer due to the exhaust flow.

Volumetric model parameters such as V_{exh} and V_{cord} in the coated GPF were determined using the geometric knowledge of the GPF design. The exhaust gas constituent volume fractions Y_i were determined from the pre-GPF λ measurements, while ρ_{O_2} and $C_{p,gas}$ were determined as a function of T_{inlet}. The cordierite specific heat capacity, $C_{p,cord}$, was obtained from parameter identification using a *clean* experimental data set that did not involve any regeneration events. Pre- and post-GPF CO_2 ppm measurements were used to determine the amount of soot oxidized, $m_{c,exp}$, during a regeneration event.

A *combined* cost function, J_C, was designed to simultaneously enhance the model prediction of thermal and soot oxidation dynamics during the parameter identification study, and the PSO algorithm was used to minimize J_C. Model validation was performed using a data set that is different from the ones used for the identification studies. The results of the temperature and soot oxidation predictions of the model were presented for two successive regeneration events in this data set.

A 1-D look-up table based on the temperature input T_{init} was used to determine the interpolated parameter values to be used in the model during validation. The computational efficiency of the model makes it suitable for OBD applications. Finally, the modeling framework presented in this paper can be easily extended to predict the internal dynamics for different washcoated GPFs.

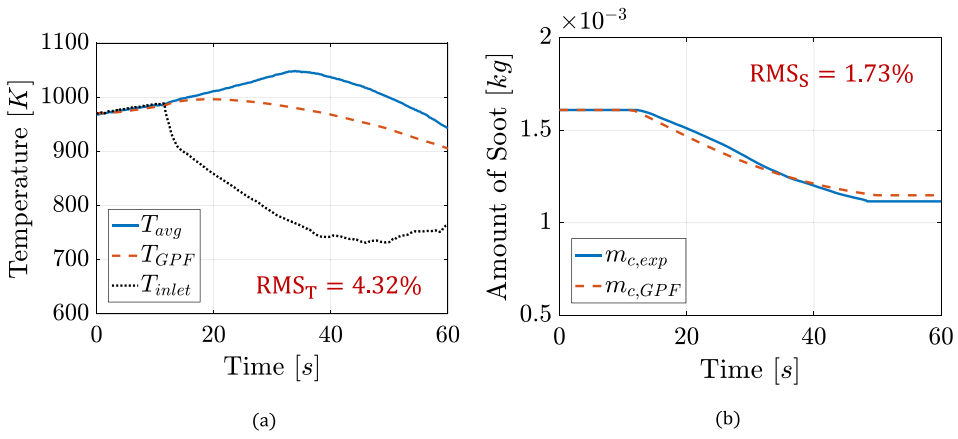

(a) (b)

Fig. 10. Model validation results illustrating the prediction of the GPF thermal and soot oxidation dynamics during Regen 1c.

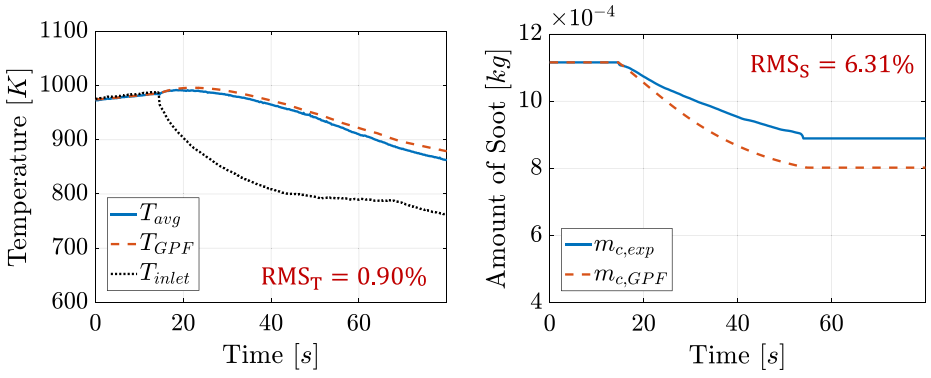

(a) (b)

Fig. 11. Model validation results illustrating the prediction of the GPF thermal and soot oxidation dynamics during Regen 2c.

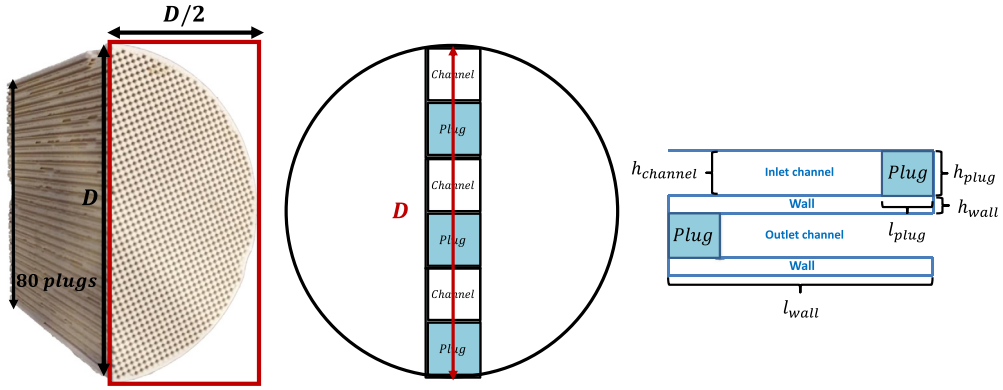

(a) (b) (c)

Fig. 12. (a) Isometric view showing the front and sectioned interior of a coated GPF. The cross-section shown here is assumed to be semi-circular, and the frontal view represents the maximum number of channels from top to bottom. Alternating channels and plugs span the entire frontal view, as shown in (b). All channels and plugs have a thickness of $(h_{channel} + h_{wall})$. (c) represents a two-dimensional view of the inlet channel, porous wall, and outlet channel.

Declaration of competing interest

The authors declare that they have no known competing financial interests or personal relationships that could have appeared to influence the work reported in this paper.

Acknowledgments

The authors gratefully acknowledge the support of Fiat Chrysler Automobiles (FCA) US LLC for granting permission to utilize experimental data from previous research collaboration. The authors would like to thank Dr. Ameya Joshi and Dr. Thorsten Boger for sharing technical insights on GPF technology which were instrumental in determining suitable parameter values for the GPF model. Responsibility for the contents of this paper lies with the authors.

Harikesh Arunachalam and Simona Onori acknowledge the financial support of National Science Foundation (NSF), United States through the CAREER Award number CMMI-1839050.

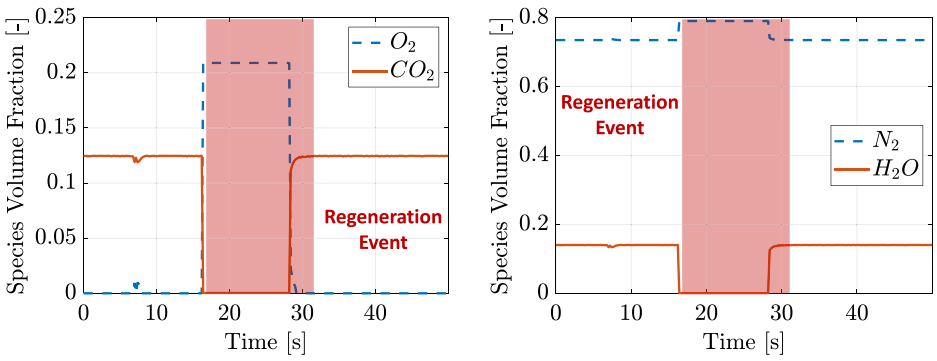

Fig. B.13. (a) Volume fraction of O_2 and CO_2 in the exhaust gas, and (b) Volume fraction of N_2 and H_2O in the exhaust gas.

Table A.11
Geometric properties of the coated GPF used in the experimental campaign of this work.

Geometric parameter	Value
Substrate diameter, D	118 [mm]
Substrate length, l_{wall}	127 [mm]
Plug length, l_{plug}	5 [mm]
Width of inlet channel, $h_{channel}$	1.26 [mm]
Total number of channels, N_{ch}	5085
Average porosity of the wall, ϕ_{wall}	0.625 [–]
Substrate volume	1.39 $\times 10^{-3}$ [m^3]
Particulate filter density, ρ_{GPF}	1100 [kg/m^3]

Appendix A. Determination of the volumetric parameters

An isometric view of the coated GPF with alternating channels and plugs is shown in Fig. 12. The number of channels is equal to the number of plugs, and the width of each channel is equal to the width of each plug. To determine V_{cord} and V_{exh}, it is essential to determine the wall thickness, h_{wall}. This value can be obtained by assuming the coated GPF to have a cylindrical shape with a circular cross-section. The first step is to determine the number of channels across the frontal semi-circular view of the sectioned GPF, N_{cross}. The geometric properties of the coated GPF are summarized in Table A.11. Assuming the GPF is composed of two identical semi-cylinders, N_{ch} can be expressed in terms of N_{cross}:

$$N_{ch} = 2 \cdot \left\{ N_{cross} \cdot \frac{N_{cross}}{2} \cdot \frac{0.5 \times \frac{\pi}{4} D^2}{D \times \frac{D}{2}} \right\}$$
$$\Rightarrow N_{cross} = \sqrt{\frac{4 \times N_{ch}}{\pi}} \approx 80 \tag{A.1}$$

The substrate diameter, D, can be expressed in terms of N_{cross} and $(h_{channel} + h_{wall})$ in the following manner:

$$D = N_{cross} \cdot (h_{channel} + h_{wall})$$
$$\Rightarrow h_{wall} = \frac{D}{N_{cross}} - h_{channel} = 0.215\ [mm]. \tag{A.2}$$

Fig. 12 (c) represents a single inlet/outlet channel pair sectioned in the axial direction. The porous walls have a volume fraction of ϕ_{wall}, and the volume fraction of the cordierite in the wall is equal to $(1 - \phi_{wall})$. The exhaust gas trapping volume inside the coated GPF, V_{exh}, is determined as:

$$\begin{aligned} V_{exh} &= N_{ch} \cdot \{(l_{wall} - l_{plug}) \cdot h_{channel} \cdot h_{channel} \\ &+ \phi_{wall} \cdot l_{wall} \cdot [h_{wall} \cdot h_{wall} + h_{wall} \cdot h_{channel} + h_{wall} \cdot h_{channel}]\} \\ &= N_{ch} \cdot \{(l_{wall} - l_{plug}) \cdot h_{channel}^2\} \\ &+ N_{ch} \cdot \{\phi_{wall} \cdot l_{wall} \cdot [h_{wall}^2 + 2 \cdot h_{wall} \cdot h_{channel}]\} \\ &= 1.222 \times 10^{-3}\ [\mathrm{m}^3] \end{aligned} \tag{A.3}$$

Similarly, the total cordierite volume, V_{cord}, is the sum of the volume of all the cordierite plugs and the sum of the volume of cordierite in all the porous walls:

$$\begin{aligned} V_{cord} &= N_{ch} \cdot \{l_{plug} \cdot h_{plug} \cdot h_{plug} + (1 - \phi_{wall}) \cdot l_{wall} \cdot \\ &\quad [h_{wall} \cdot h_{wall} + h_{wall} \cdot h_{channel} + h_{wall} \cdot h_{channel}]\} \\ &= N_{ch} \cdot \{l_{plug} \cdot h_{plug}^2 + (1 - \phi_{wall}) \cdot l_{wall} \cdot \\ &\quad [h_{wall}^2 + 2 \cdot h_{wall} \cdot h_{channel}]\} \\ &= 0.1828 \times 10^{-3}\ [\mathrm{m}^3] \end{aligned} \tag{A.4}$$

The sum of V_{exh} and V_{cord} for the coated GPF used in this study is 1.4048 $\times 10^{-3}$ [m^3], a value that is approximately equal to the volume encompassed by the exterior geometric dimensions of the coated GPF substrate.

Appendix B. Determination of the exhaust gas parameters

The reaction rate expressions (9) and (11), the soot oxidation dynamic equation (22), and the mass fraction variation equation of available ceria sites (23) depend on the volume fraction of oxygen, Y_{O_2}. Under nominal operating conditions, Y_{O_2} is set to zero by assuming near stoichiometric combustion of gasoline and a properly functioning TWC upstream of the GPF. In order to initiate a regeneration event within the GPF, the engine is forced to operate under lean conditions where the air–fuel ratio, λ, measured using a wide range lambda sensor, is greater than the stoichiometric value of 1. As a result, the concentration of oxygen inside the GPF increases and initiates reaction pathways (2), (4), and (5).

As the internal GPF temperature increases, these reaction rates are enhanced, leading to an accelerated oxidation of the trapped soot. For this investigation, Y_{O_2} is computed using the air–fuel ratio measurements provided by a wide range lambda sensor mounted upstream of the GPF, and the kinetics of the following combustion reaction (Heywood, 1988):

$$C_a H_b + \lambda\left(a + \tfrac{b}{4}\right)(O_2 + 3.773 N_2) \rightarrow$$
$$a CO_2 + \tfrac{b}{2} H_2O + \lambda \cdot 3.773 \cdot \left(a + \tfrac{b}{4}\right) N_2 + (\lambda - 1)\left(a + \tfrac{b}{4}\right) O_2 \tag{B.1}$$

The total number of product moles in the above equation is:

$$n_{total} = a + \frac{b}{2} + \lambda \cdot 3.773 \cdot \left(a + \frac{b}{4}\right) + (\lambda - 1)\left(a + \frac{b}{4}\right) \tag{B.2}$$

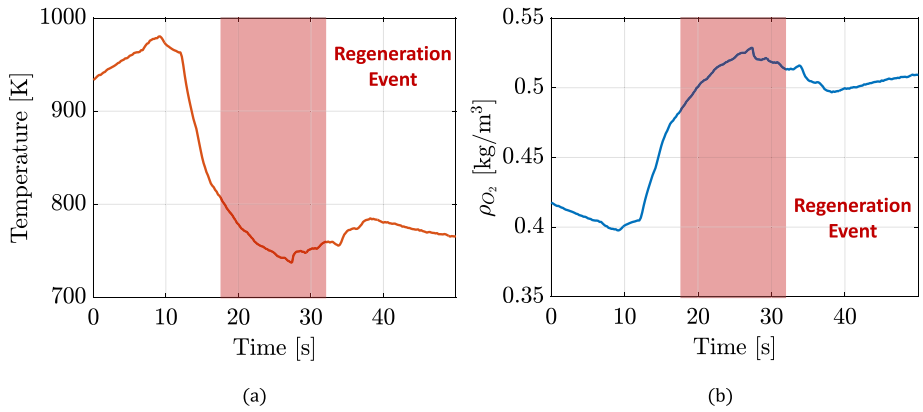

Fig. B.14. (a) GPF inlet exhaust gas temperature (measured), and (b) variation of the O_2 gas density with time (calculated using Eq. (B.6)).

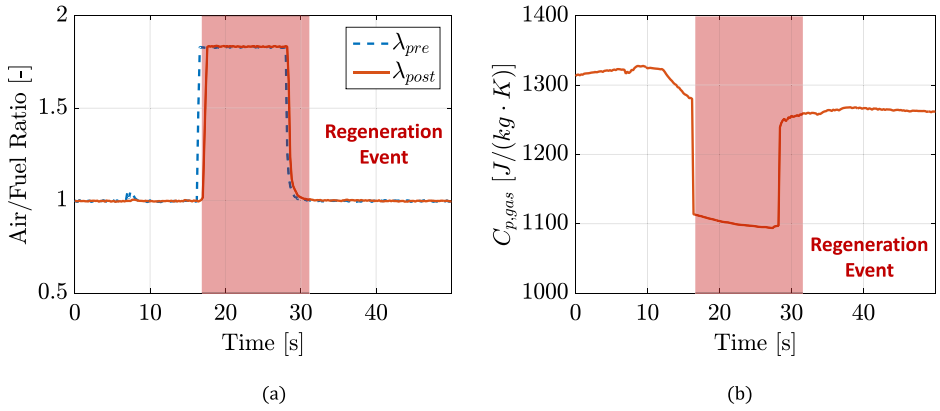

Fig. B.15. (a) Pre- and post-GPF air–fuel ratio, and (b) variation in the specific heat capacity of the exhaust gas with time. The GPF inlet exhaust gas temperature illustrated in Fig. B.14 (a) is used to calculate $C_{p,gas}$ using Eq. (B.7).

Considering $C_aH_b = C_8H_{18}$ (octane), the volume fraction of each constituent gas species is determined as the ratio of the moles of that particular species to the total number of moles of combustion products:

$$Y_{N_2} = \lambda \cdot \frac{3.773 \times \left(a + \frac{b}{4}\right)}{n_{total}}, \; Y_{O_2} = \frac{(\lambda - 1) \cdot \left(a + \frac{b}{4}\right)}{n_{total}},$$

$$Y_{CO_2} = \frac{a}{n_{total}}, \text{ and } Y_{H_2O} = \frac{\left(\frac{b}{2}\right)}{n_{total}} \tag{B.3}$$

Fig. B.13 presents the volume fraction of each exhaust gas constituent during the regeneration event described earlier in Section 3.1. When the fuel-cut event occurs, the volume fraction of O_2 in the exhaust gas is set to that of atmospheric air, 0.209 (Zannis, Pariotis, Hountalas, Rakopoulos, & Levendis, 2007), and the regeneration event begins. Due to the ceria's oxygen storage capability, the regeneration event may be elongated beyond the time when Y_{O_2} drops to 0.0 at the GPF inlet.

The mass of oxygen trapped inside the coated GPF, m_{O_2}, is equal to $\rho_{O_2} \cdot Y_{O_2} \cdot V_{exh}$. Oxygen density ρ_{O_2} is determined as a function of T_{inlet} using the ideal gas equation:

$$P_{O_2} \cdot V_{O_2} = n_{O_2} \cdot R \cdot T_{inlet} \tag{B.4}$$

Converting V_{O_2} and n_{O_2} in terms of mass and density terms, the above equation can be reformulated as:

$$P_{O_2} \cdot \left(\frac{m_{O_2}}{\rho_{O_2}}\right) = \left(\frac{m_{O_2}}{M_{O_2}}\right) \cdot R \cdot T_{inlet} \tag{B.5}$$

The density of oxygen, ρ_{O_2}, can then be expressed as:

$$\rho_{O_2} = \frac{P_{O_2} \cdot M_{O_2}}{R \cdot T_{inlet}} \tag{B.6}$$

Since the proposed model utilizes the temperature of the exhaust gas at the inlet of the GPF, it is appropriate to determine the density of oxygen at this location. Exhaust gas pressure at the GPF inlet is assumed to be equal to atmospheric pressure. Fig. B.14(a) presents the exhaust gas temperature profile at the GPF inlet for the regeneration event described in Section 3.1. For this temperature profile, the variation in the oxygen density with time is presented in Fig. B.14(b).

$C_{p,gas}$ is determined as a function of T_{inlet} using the volume fraction of each constituent gas species (N_2, O_2, CO_2, and H_2O):

$$\begin{aligned} C_{p,gas} = {} & Y_{N_2} \cdot C_{p,N_2}(T_{inlet}) + Y_{O_2} \cdot C_{p,O_2}(T_{inlet}) \\ & + Y_{CO_2} \cdot C_{p,CO_2}(T_{inlet}) + Y_{H_2O} \cdot C_{p,H_2O}(T_{inlet}), \end{aligned} \tag{B.7}$$

where $C_{p,N_2}(T_{inlet})$, $C_{p,O_2}(T_{inlet})$, $C_{p,CO_2}(T_{inlet})$, and $C_{p,H_2O}(T_{inlet})$ are specific heat capacities of the individual exhaust gas constituents. Their values as a function of temperature are provided in the NIST-JANAF tables (Chase, 1998). Using this information, the constituent gas specific heat capacities can be determined as a function of the GPF inlet exhaust gas temperature.

Fig. B.15 illustrates a representative variation in exhaust gas heat capacity during a regeneration event. The decrease in the overall specific heat capacity is due to a decrease in the volume fraction of triatomic molecules, CO_2 and H_2O, whose more complex molecular structures have a greater number of vibrational and rotational modes to absorb energy than the simpler, diatomic molecular structures of N_2 and O_2.

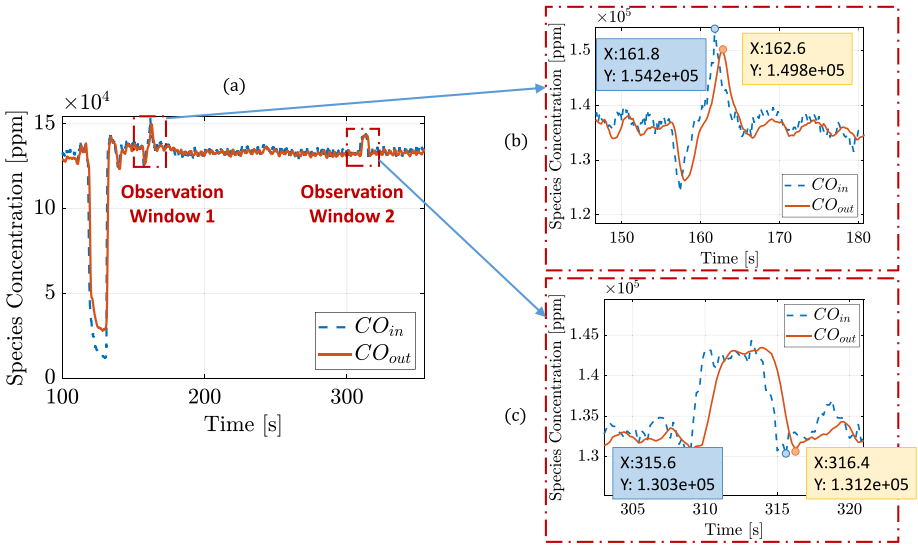

Fig. C.16. (a) Raw measurements of pre and post-GPF CO_2 ppm levels with the observation windows highlighted, (b) magnified view of observation window 1, and (c) magnified view of observation window 2.

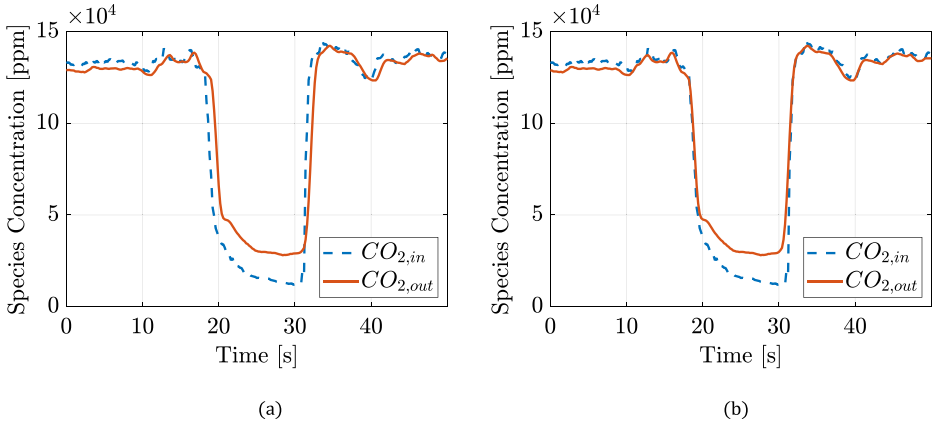

Fig. C.17. (a) Pre and post-GPF CO_2 ppm levels before shifting (original data), and (b) CO_2 ppm level measurements after shifting the post-GPF CO_2 ppm by 0.8 s.

Appendix C. Determination of the soot mass oxidized, $m_{c,exp}$, during regeneration

The experimental measurements of CO_2 ppm levels are processed to account for time delays associated with exhaust gas transport through the GPF and the FTIR analyzer. The following sequence of steps are implemented before determining the amount of soot oxidized during a regeneration event:

1. Temporally shift the post-GPF CO_2 ppm data to align with the pre-GPF CO_2 ppm data. This shift eliminates the transport time taken for exhaust gas flow through the GPF.
2. Temporally shift pre- and post-GPF CO_2 ppm measurements to correlate the measured data with the onset of a regeneration event. This shift eliminates the transport delay associated with exhaust gas flow through transport lines to the FTIR analyzer.

Since the transport lines for both pre- and post-GPF ppm measurements are of the same length and both analyzers use the same flow rate, both pre- and post-GPF CO_2 measured data are shifted by the same amount. After employing this shift, the FTIR species concentration data more accurately aligns with the mass flow and lambda signals.

Using the raw measured CO_2 ppm data, two time windows were observed to understand the magnitude of the time shift required. This is illustrated in Fig. C.16. During nominal engine operation, the pre- and post-GPF CO_2 ppm measurements must be nearly equal. The time instant at which the pre and post-GPF CO_2 ppm levels reached a peak/trough were analyzed. The post-GPF measurements achieved their corresponding peak/trough value with a 0.8 s time delay with respect to their pre-GPF counterparts. Hence, this value was chosen to perform the time shift in step 1. The CO_2 ppm levels after this implementation are shown in Fig. C.17.

To perform step 2, the start and end time of the regeneration event must be first identified. The start time, t_s, is chosen as the first time instance when the post-GPF CO_2 ppm level, $CO_{2,out}$, exceeds the pre-GPF CO_2 ppm level, $CO_{2,in}$. The end time, t_f, is chosen as the first time instance when $CO_{2,in}$ exceeds $CO_{2,out}$ during the rise in ppm levels. As shown in Fig. C.18(a), t_s is equal to 18.4 s and t_f is equal to 31.6 s. Time t_m is chosen as the instant when the pre-GPF air–fuel ratio curve first reaches its maximum measured value. As shown in Fig. C.18(b), $t_m = 16.6$ s.

Both pre- and post-GPF CO_2 ppm data are shifted by the same amount such that the start time of regeneration matches time t_m. In this case, the pre- and post-GPF ppm measurements are shifted by $(t_s - t_m)$, or 1.8 s. With this time shift employed, Y_{O_2} is equal to 0.209 as soon as the regeneration event begins.

It is assumed that no soot is oxidized during nominal engine operation conditions, when the post TWC λ is at the stoichiometric value of 1. During the regeneration event, $m_{c,exp}$, which represents the amount

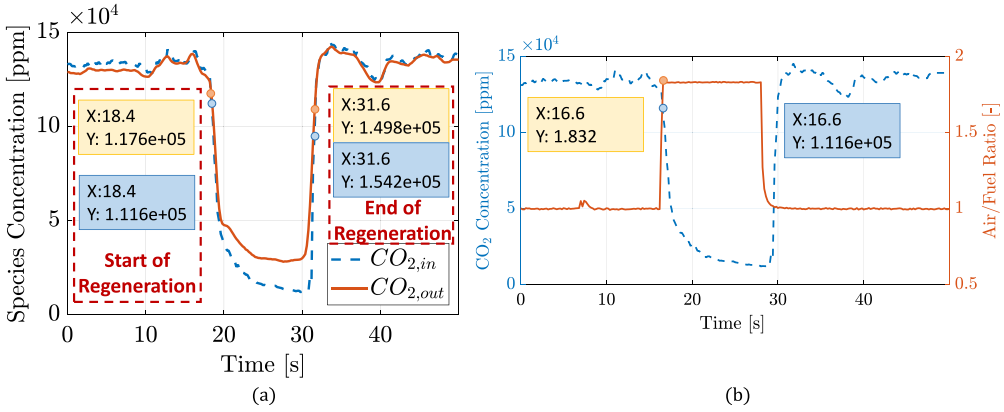

Fig. C.18. (a) Approach to determine the start and end time of the regeneration event, and (b) pre-GPF CO_2 ppm measurements with respect to the pre-GPF air–fuel ratio after a shift of 1.8 s to the left.

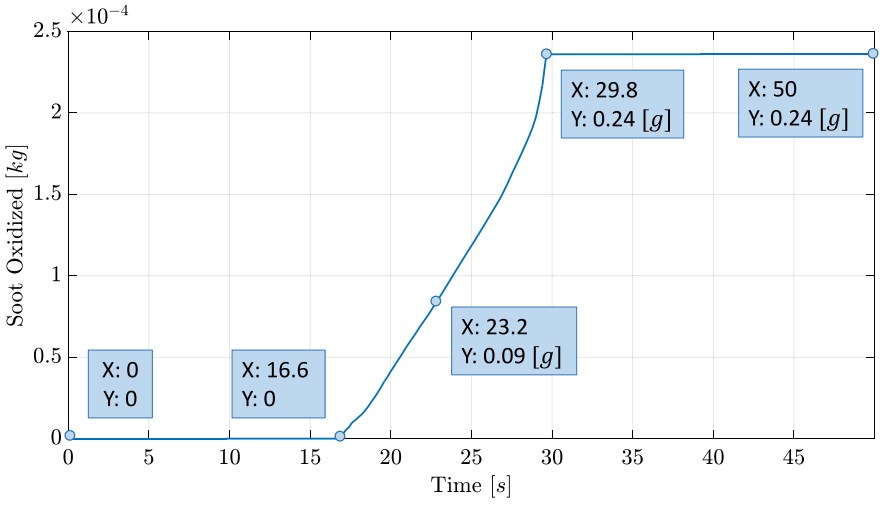

Fig. C.19. The amount of soot oxidized as a function of time during the regeneration event illustrated in Fig. C.18(a).

of soot oxidized, is calculated using the expression:

$$m_{c,exp,end} = m_{c,exp,ini} + \int_{t_s}^{t_f} \left(CO_{2,out} - CO_{2,in}\right) \cdot 10^{-6} \times \dot{m}_g \times \left(\frac{M_C}{M_{CO_2}}\right) \cdot dt \tag{C.1}$$

Once the pre- and post-GPF CO_2 ppm levels are shifted with respect to the pre-GPF λ, t_s and t_f become 16.6 s and 29.8 s, respectively. The experimental data presented in this paper have been measured in time steps of $\Delta t = 0.2$ s. Eq. (C.1) can then be expressed in discrete time as:

$$m_{c,exp,end} = m_{c,exp,ini} + \sum_{i=1}^{M} \left(CO_{2,out}(i) - CO_{2,in}(i)\right) \cdot 10^{-6} \times \dot{m}_g(i) \times \left(\frac{M_C}{M_{CO_2}}\right) \cdot \Delta t, \tag{C.2}$$

where $M = (t_f - t_s)/\Delta t = 66$. Then, $m_{c,exp}$ at any time step $(j+1)$ can be expressed in terms of $m_{c,exp}$ at time step j:

$$m_{c,exp}(j+1) = m_{c,exp}(j) + \left[\left(CO_{2,out}(j) - CO_{2,in}(j)\right) \cdot 10^{-6} \times \dot{m}_g(j) \times \left(\frac{M_C}{M_{CO_2}}\right) \cdot \Delta t\right] \tag{C.3}$$

The experimental data set presented in Fig. C.18(a) is 50 s long. The following considerations have been made:

1. From time $t = 0$ s to time $t = t_s$, it is assumed that there is no soot oxidation ($m_{c,exp} = m_{c,exp,ini} = 0$).
2. From time $t = t_s$ to time $t = t_f$, soot oxidation occurs due to regeneration, and $m_{c,exp}$ is calculated at every time instant using Eq. (C.3).
3. From time $t = t_f$ to time $t = 50$ s, it is assumed that there is no soot oxidation ($m_{c,exp} = m_{c,exp,end}$).

The amount of soot oxidized, $m_{c,exp}$, for the experimental data presented in Fig. C.18(a) is schematically represented in Fig. C.19. The total amount of soot oxidized during this regeneration event is equal to 0.24 [g].

Appendix D. Parameter identification results using the thermal and soot cost functions

The objective of the *thermal* cost function is to minimize the error between the experimental and model-predicted GPF temperature values during the identification process. Mathematically, this cost function, J_T, is defined as:

$$J_T(\theta) = \sqrt{\frac{1}{N}\sum_{i=1}^{N}\left(T_{avg}(i) - T_{GPF}(\theta;i)\right)^2} \cdot \frac{100}{\max(T_{avg})} \tag{D.1}$$

Fig. D.20 presents the parameter identification results using the *thermal* cost function. The RMS_T and RMS_S values obtained from this identification are respectively 0.92% and 10.33%. This identification study completely emphasizes the minimization of the thermal RMS

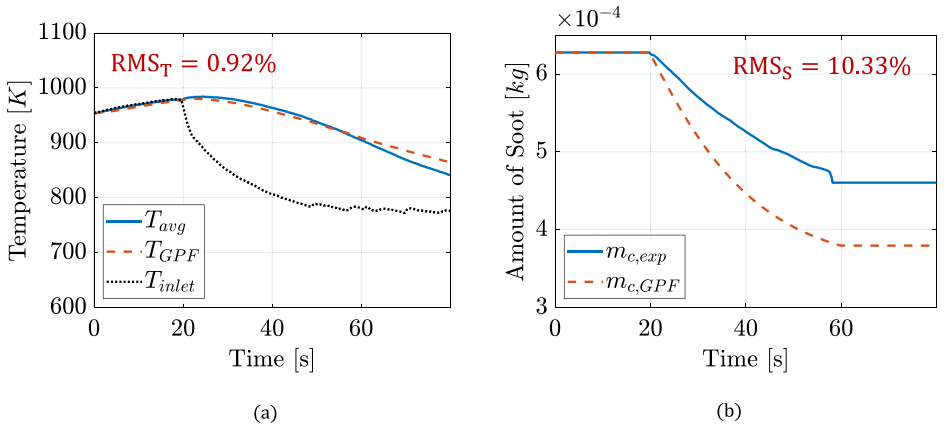

Fig. D.20. Identification results using the *thermal* cost function to evaluate the (a) thermal and (b) soot oxidation response of the model.

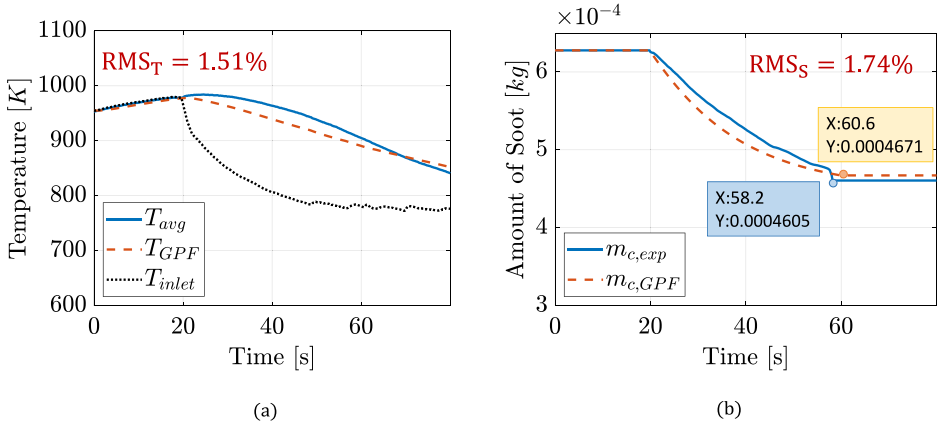

Fig. D.21. Identification results using the *soot* cost function to evaluate the (a) thermal and (b) soot oxidation response of the model.

error without including soot oxidation in the cost function. It is possible in such cases to identify parameters which yield large values of RMS$_S$.

The objective of the *soot* cost function during the identification process is to minimize the error between the experimental and model-predicted mass of soot oxidized during a regeneration event. Mathematically, this cost function, J_S, is defined as:

$$J_S(\theta) = \sqrt{\frac{1}{N}\sum_{i=1}^{N}\left(m_{c,exp}(i) - m_{c,GPF}(\theta;i)\right)^2} \cdot \frac{100}{\max(m_{c,exp})} \tag{D.2}$$

Fig. D.21 presents parameter identification results using the *soot* (carbon balance) cost function. The RMS$_T$ and RMS$_S$ values obtained from this identification are respectively 1.51% and 1.74%.

References

Arunachalam, H., Pozzato, G., Hoffman, M. A., & Onori, S. (2017). Modeling the thermal dynamics inside a ceria-coated gasoline particulate filter. In *Conference on control technology and applications* (pp. 99–105). IEEE.

Atkins, P., et al. (2014). *Physical chemistry: thermodynamics, structure, and change*. Macmillan Higher Education.

Boger, T., Rose, D., Nicolin, P., Gunasekaran, N., & Glasson, T. (2015). Oxidation of Soot (Printex® U) in particulate filters operated on gasoline engines. *Emission Control Science and Technology*, *1*(1), 49–63.

Cengel, Y. A., & Boles, M. A. (2002). *Thermodynamics: an engineering approach*. McGraw-Hill Education.

Chan, T. W., Meloche, E., Kubsh, J., Rosenblatt, D., Brezny, R., & Rideout, G. (2012). Evaluation of a gasoline particulate filter to reduce particle emissions from a gasoline direct injection vehicle. *SAE International Journal of Fuels and Lubricants*, *5*(2012-01-1727), 1277–1290.

Chase, M. (1998). NIST-JANAF thermochemical tables. *Journal of Physical and Chemical Reference Data Monograph*, (9).

Chiatti, G., Chiavola, O., & Falcucci, G. (2008). Lumped parameter approach for DPF management in stationary diesel engines. In *ASME 2008 internal combustion engine division spring technical conference* (pp. 75–85). American Society of Mechanical Engineers.

National Research Council (2011). Assessment of fuel economy technologies for light-duty vehicles. *Tech. rep.*, National Academies Press.

Depcik, C., Langness, C., & Mattson, J. (2014). Development of a simplified diesel particulate filter model intended for an engine control unit. *Tech. rep. 2014-01-1559*, SAE Technical Paper.

Ebbesen, S., Kiwitz, P., & Guzzella, L. (2012). A generic particle swarm optimization matlab function. In *American control conference* (pp. 1519–1524). IEEE.

Gong, J., Stewart, M. L., Zelenyuk, A., Strzelec, A., Viswanathan, S., Rothamer, D. A., Foster, D. E., & Rutland, C. J. (2018). Importance of filter's microstructure in dynamic filtration modeling of gasoline particulate filters (GPFs): Inhomogeneous porosity and pore size distribution. *Chemical Engineering Journal*, *338*, 15–26.

Hassanpour, S., & McPhee, J. (2018). A control-oriented modular one-dimensional model for wall-flow diesel particulate filters. *International Journal of Engine Research*, *19*(3), 329–346.

Heywood, J. (1988). *Internal combustion engine fundamentals*. McGraw-Hill Education.

Ito, Y., Shimoda, T., Aoki, T., Yuuki, K., Sakamoto, H., Kato, K., Thier, D., Kattouah, P., Ohara, E., & Vogt, C. (2015). Next generation of ceramic wall flow gasoline particulate filter with integrated three way catalyst. *Tech. rep.*, SAE Technical Paper.

Johnson, T., & Joshi, A. (2017). Review of vehicle engine efficiency and emissions. *Tech. rep.*, SAE Technical Paper.

Khalek, I. A., Bougher, T., & Jetter, J. J. (2010). Particle emissions from a 2009 gasoline direct injection engine using different commercially available fuels. *SAE International Journal of Fuels and Lubricants*, *3*(2010-01-2117), 623–637.

Konstantas, G., & Stamatelos, A. (2004). Computer aided engineering of diesel filter systems. In *Joint meeting of the Italian and the Greek section of the combustion institute* (pp. 17–19).

Korneev, S., & Onori, S. (2018). Modeling the transport dynamics in gasoline particulate filters. In *ASME 2018 dynamic systems and control conference* (pp. V002T26A002–V002T26A010).

Kostoglou, M., & Konstandopoulos, A. G. (2005). Effect of soot layer microstructure on diesel particulate filter regeneration. *AIChE Journal*, *51*(9), 2534–2546.

Lambert, C., Chanko, T., Dobson, D., Liu, X., & Pakko, J. (2017). Gasoline particle filter development. *Emission Control Science and Technology*, *3*(1), 105–111.

Lide, D. R., & Haynes, W. M. (2009). *CRC handbook of chemistry and physics: a ready-reference book of chemical and physical data*. Boca Raton, FLA: CRC.

Liu, X., Kim, J., Chanko, T., Lambert, C., & Pakko, J. (2017). A modeling analysis of fibrous media for gasoline particulate filters. *Tech. rep. 2017-01-0967*, SAE Technical Paper.

Mamakos, A., Martini, G., Dilara, P., & Drossinos, Y. (2011). Feasibility of introducing particulate filters on gasoline direct injection vehicles. *Tech. rep.*, Citeseer, JRC Scientific and Policy Report, EU Commission.

Morgan, C. (2015). Platinum group metal and washcoat chemistry effects on coated gasoline particulate filter design. *Johnson Matthey Technology Review*, *59*(3), 188–192.

Nicolin, P., Rose, D., Kunath, F., & Boger, T. (2015). Modeling of the soot oxidation in gasoline particulate filters. *SAE International Journal of Engines*, *8*(2015-01-1048), 1253–1260.

Opitz, B., Drochner, A., Vogel, H., & Votsmeier, M. (2014). An experimental and simulation study on the cold start behaviour of particulate filters with wall integrated three way catalyst. *Applied Catalysis B: Environmental*, *144*, 203–215.

Pozzato, G., Hoffman, M. A., & Onori, S. (2017). Multi-channel physics-based modeling and experimental validation of an uncoated gasoline particulate filter in clean operating conditions. In *American control conference* (pp. 5392–5397). IEEE.

Rathod, D., Onori, S., Filipi, Z., & Hoffman, M. (2018). Experimental investigation of soot accumulation and regeneration in a catalyzed gasoline particulate filter using particle quantification and gas speciation measurements. In *ASME 2018 internal combustion engine fall technical conference*.

Rounce, P., Brogan, M., & Eastwood, P. (2013). Gasoline direct injected particulate emissions control at stage 6. In IMechE (Ed.), *Internal combustion engines: performance, fuel economy and emissions* (pp. 231–250). Woodhead Publishing.

Shimoda, T., Ito, Y., Saito, C., Nakatani, T., Shibagaki, Y., Yuuki, K., Sakamoto, H., Vogt, C., Matsumoto, T., Furuta, Y., et al. (2012). Potential of a low pressure drop filter concept for direct injection gasoline engines to reduce particulate number emission. *Tech. rep.*, SAE Technical Paper.

Takahashi, A., Korneev, S., & Onori, S. (2019). Sensitivity study on thermal and soot oxidation dynamics of gasoline particulate filters. In *2019 SAE world congress*.

Whitaker, P., Kapus, P., Ogris, M., & Hollerer, P. (2011). Measures to reduce particulate emissions from gasoline DI engines. *SAE International Journal of Engines*, *4*(2011-01-1219), 1498–1512.

Williams, J. L. (2001). Monolith structures, materials, properties and uses. *Catalysis Today*, *69*(1–4), 3–9.

Wu, Y., Zhang, S., Hao, J., Liu, H., Wu, X., Hu, J., Walsh, M. P., Wallington, T. J., Zhang, K. M., & Stevanovic, S. (2017). On-road vehicle emissions and their control in China: A review and outlook. *Science of The Total Environment*, *574*, 332–349.

Yang, S., Deng, C., Gao, Y., & He, Y. (2016). Diesel particulate filter design simulation: A review. *Advances in Mechanical Engineering*, *8*(3), 1–14.

Zaman, K., & Abd-el Moemen, M. (2017). Energy consumption, carbon dioxide emissions and economic development: evaluating alternative and plausible environmental hypothesis for sustainable growth. *Renewable and Sustainable Energy Reviews*, *74*, 1119–1130.

Zannis, T. C., Pariotis, E. G., Hountalas, D. T., Rakopoulos, D. C., & Levendis, Y. A. (2007). Theoretical study of DI diesel engine performance and pollutant emissions using comparable air-side and fuel-side oxygen addition. *Energy Conversion and Management*, *48*(11), 2962–2970.

Zhu, R., Hu, J., Bao, X., He, L., Lai, Y., Zu, L., Li, Y., & Su, S. (2016). Tailpipe emissions from gasoline direct injection (GDI) and port fuel injection (PFI) vehicles at both low and high ambient temperatures. *Environmental Pollution*, *216*, 223–234.